

POLITECNICO DI TORINO

Corso di Laurea Magistrale in Ingegneria Elettronica

Tesi di Laurea Magistrale

**Tunable Silicon Photonic lasers  
exploiting ring resonators:  
overview and modelization**



Relatori:

Prof. Mariangela GIOANNINI

Prof. Lorenzo COLUMBO

Dott.sa Cristina RIMOLDI

Candidato:

Chiara PETOLICCHIO

Aprile 2023

# Abstract

Thanks to its important features in the field of integrated electronic circuits and CMOS processes, Silicon is one of the most used semiconductor in electronic industry.

Actually, research is moving in the direction of using this material also for photonic application, trying to integrate photonic devices over semiconductor platforms, with the purpose to improve integrated circuits performances, for example increasing transmission velocity.

Silicon Photonics studies how efficiently embed photonic components in silicon integrated circuits. The main drawback of using Silicon-based technology in photonic circuits, is that Silicon is an indirect band-gap semiconductor, this means that it is not perfectly suitable to fabricate active optical devices, like lasers, since during recombination processes there is not energy-momentum conservation. For this reason, in this thesis integration technologies of photonic devices are firstly analysed, pointing out benefits and drawbacks of monolithic and heterogeneous integration methods, focusing then on platforms that can guarantee effective integration, and are always scalable and CMOS compatible, including SiO<sub>2</sub>, Silicon Nitride and Indium Phosphide platforms.

The state of the art currently proposes solutions for Silicon Photonic mainly with heterogeneous integration, ensuring that the performance of lasers are satisfactory in terms of very narrow linewidth, suitably high optical power output and very low losses. In order to achieve these goals, two research groups are analysed, which have in common the use of ring resonators as resonant cavities in lasers, which are useful to increase the effective cavity length, favouring light emission with very narrow linewidth and, above all, making the laser tunable guaranteeing a wide frequency span of the emitted light.

The purpose of this thesis is to simulate the static and dynamic behaviour of an integrated laser on a Silicon Nitride platform, consisting of a reflective outer section, waveguide, phase section and two coupled ring resonators. In particular, the emission spectrum was obtained, the device's response to a current intensity modulation (small-signal) has been simulated, the Relative Intensity Noise (RIN) and the spectrum of the integrated RIN were retrieved. Finally, the dynamic behaviour of the laser has been analysed by plotting the eye diagram stimulating the laser with square wave modulation of current and a pseudo-random bit stream. Each simulation has been done for different coupling coefficient values, producing different FWHM values.

---

In conclusion, the structure analysed and simulated is confirmed as a valid possibility for the integration of optoelectronic devices on Silicon. In fact, the dynamic and static behaviour of the device is satisfactory and comparable with the state of the art, so the characteristic of the analysed device are promising. Considering the compatibility of materials taken in consideration with the CMOS process, good scalability characteristics are also guaranteed. The analysis performed can be developed and extended by considering other non-linear effects introduced by the use of Silicon, e.g. the Kerr Effect and Two-Photon Absorption, so that more realistic simulations can be performed.

# Table of contents

<b>1</b>	<b>Introduction</b>	<b>1</b>
1.1	Semiconductors for optoelectronic applications . . . . .	1
1.1.1	Direct band gap semiconductors . . . . .	1
1.1.2	Indirect band gap semiconductors . . . . .	2
1.2	Why Silicon Photonics? . . . . .	3
1.3	Monolithically integrated circuits . . . . .	4
1.4	Heterogeneously integrated circuits . . . . .	7
1.4.1	Optical Interconnections . . . . .	8
1.4.2	Passive Optical Components . . . . .	8
1.4.3	Active Optical Components . . . . .	9
1.5	Hybrid Integrated Circuits . . . . .	10
1.6	Platforms for Silicon Photonics . . . . .	10
1.6.1	Silicon-On-Insulator Platform . . . . .	11
1.6.2	SiN-on-Silica Platform . . . . .	12
1.6.3	InP Platform . . . . .	13
<b>2</b>	<b>State of the Art</b>	<b>14</b>
2.1	John E. Bowers research group . . . . .	14
2.2	Klaus J. Boller research group . . . . .	25
2.3	Comparison . . . . .	32
<b>3</b>	<b>Simulations</b>	<b>33</b>
3.1	Structure . . . . .	33
3.2	Mathematical model . . . . .	35
3.3	Dynamical Simulations . . . . .	37
3.3.1	Intensity Modulation response . . . . .	38
3.3.2	Relative Intensity Noise (RIN) spectrum . . . . .	43
3.3.3	Integrated RIN . . . . .	46
3.3.4	Eye Diagram . . . . .	48
<b>4</b>	<b>Conclusions</b>	<b>55</b>

# List of figures

1.1	Direct band-gap semiconductor versus Indirect band-gap semiconductor[2]	2
1.2	Moore's law for photonics [5]	5
1.3	Optical transmission windows	9
1.4	Fabrication process of SOI wafer, property of SOITEC.[10]	11
2.1	E-DBR laser and RAE-DBR laser	15
2.2	Light-Current-Voltage characteristic E-DBR.	17
2.3	Light-Current characteristic RAE-DBR.	17
2.4	Multi-mode regions.	18
2.5	Structure of multiring laser.	19
2.6	Three-block scheme with simplification.	21
2.7	Detuned Loading effect [16]	22
2.8	Structure of the first generation of laser.	23
2.9	Structure of the second generation of laser.	24
2.10	Structure of hybrid integrated laser.	26
2.11	Frequency comb spectrum.	27
2.12	Structure of hybrid integrated laser.	29
2.13	Photon lifetime.	30
2.14	Output spectrum.	31
3.1	Hybrid laser structure.	34
3.2	IM response for different FWHM.	38
3.3	IM response at FWHM=6.2GHz for different values of $\Delta\nu$	39
3.4	IM response at FWHM=6.2GHz for negative values of $\Delta\nu$	40
3.5	IM response at FWHM=6.2GHz for positive values of $\Delta\nu$	40
3.6	IM response at FWHM=1GHz for different values of $\Delta\nu$ .	41
3.7	IM response at FWHM=9GHz for different values of $\Delta\nu$ .	42
3.8	IM response at FWHM=11GHz for different values of $\Delta\nu$ .	42
3.9	IM response at FWHM=20GHz for different values of $\Delta\nu$ .	43
3.10	RIN spectrum for $\Delta\nu = -2.65GHz$	44
3.11	RIN spectrum for $\Delta\nu = -4.24GHz$	45
3.12	RIN spectrum for $\Delta\nu = 2.69GHz$	45
3.13	Integrated RIN for FWHM=1GHz	46
3.14	Integrated RIN for FWHM=3GHz	47
3.15	Integrated RIN for FWHM=6.2GHz	47
3.16	Integrated RIN for FWHM=9GHz	48
3.17	Eye Diagram with modulation frequency of 10 GHz.	49

3.18	Eye Diagram with modulation frequency of 20 GHz. . . . .	50
3.19	Eye Diagram with modulation frequency of 30 GHz. . . . .	51
3.20	Current vs Time. . . . .	52
3.21	Closeup of the previous current vs time plot. . . . .	53
3.22	Eye Diagram with Pseudo Random Bit Stream of Current and Frequency=10GHz. . . . .	54

# Chapter 1

## Introduction

During the past decades, since the invention of the transistor, research has done many steps forward in the direction of optimizing devices' performances through the study of electronic processes and materials, in particular Silicon, the peculiar electronic properties of which guaranteed the leading position in the field of semiconductors for electronic devices.

### 1.1 Semiconductors for optoelectronic applications

In more recent years research has moved in the direction of the study of semiconductors for optoelectronic applications; unfortunately the most used material, Si, was not able to guarantee an equal success in this field, being an indirect band gap semiconductor, as illustrated in the following, leading to the use of semiconductor compounds to overcome these physical limitations.

In semiconductors the allowed states for electrons that are obtained through the Schroedinger's equations forms not discrete energy levels, but two continuous energy bands [1]. These two bands are the *Conduction energy band* and *Valence energy band*, the energy separation between these two is called *Energy gap*  $E_g$ . The optical processes that happens in the semiconductor depends strictly on how these bands are positioned, if they are aligned or not and on their characteristics, this is shown in details in Fig.1.1.

#### 1.1.1 Direct band gap semiconductors

If the maximum of the valence band is aligned with the minimum of the conduction band the semiconductor is referred to as *Direct band-gap*, and it means that the k-vector, the *crystal momentum* of electrons and holes, is the same both in conduction

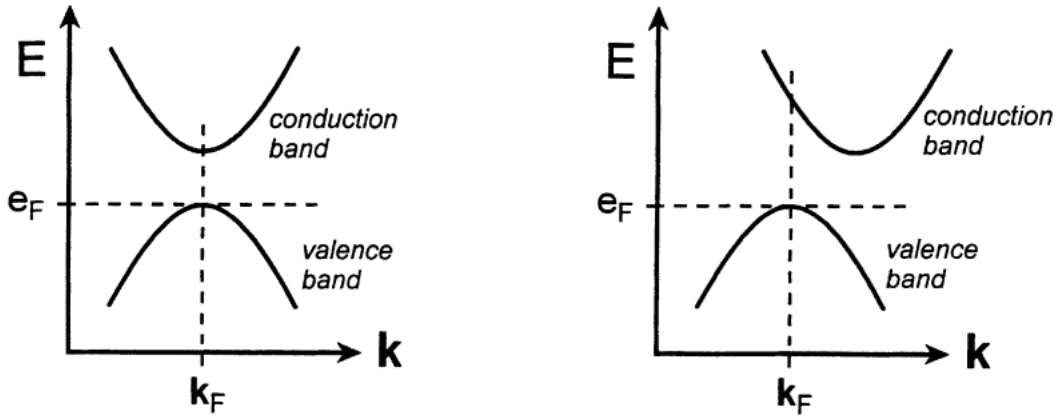


Figure 1.1: Direct band-gap semiconductor versus Indirect band-gap semiconductor[2]

and valence band. Many semiconductors are in this category, including amorphous Silicon and III-V semiconductor compounds.

Materials in this category are particularly important for optoelectronic purposes, since they can interact directly with photons that can provide the energy needed to promote electrons from Valence band to the Conduction band, still maintaining the energy-momentum relation, also called *dispersion relation*  $E(k)$ , so without changes in the k-vector[3].

### 1.1.2 Indirect band gap semiconductors

On the other hand, if the minimum of the conduction band is not aligned with the maximum of the valence band the semiconductor is called *Indirect band-gap*. In this case the crystal momentum (k) is different in the two energy bands.

In this situation interactions between photons and electrons require a large amount of momentum, that the photons are not able to provide, for this reason in this interaction are involved also lattice vibrations (*phonons*).

Since three particles are involved, i.e. an electron, a photon, and a phonon, the process occurs at a slower rate than in the case of direct band gap semiconductors. Moreover it is worth to specify that in Silicon, and in general in indirect band gap semiconductors, two important non-radiative recombination processes are involved:

Auger recombination and Free Carrier Absorption (FCA). In particular, the first one i.e. the Auger phenomenon, is a non-radiative recombination process, meaning that light will not be emitted as a consequence of the recombination of a hole-electron pair. The Auger recombination phenomenon happens when there is the creation of an electron-hole pair, but the excess energy instead of giving rise to a photon, is transferred to carriers, i.e. electrons or holes, that will be excited to higher energy levels inside the energy band.

The recombination rate due to this phenomenon, for both carriers, will be:

$$R_A = C_e n^2 p \quad R_A = C_h p^2 n \quad (1.1)$$

If the electron density and hole density are equal, this recombination rate will be:

$$R_A = C n^3 \quad (1.2)$$

In which  $C = C_e + C_h$ . In materials with large band-gap this effect is quite negligible, while in semiconductors with sufficiently small band-gap, where the Auger recombination is relevant, it will impact lasing for increasing currents.

The other mentioned phenomenon is the Free Carrier Absorption (FCA), it is an *Intraband absorption* effect, which occurs when a semiconductor absorbs an incident photon and a carrier laying on an already excited state is then excited to an higher energy level still in the same energy band.

## 1.2 Why Silicon Photonics?

The continuous expansion of the technological research led to focus the attention on integrability of optoelectronic components in Silicon platforms. Having different optical elements in a single photonic integrated circuit means that light is guided through waveguides and other components on the same planar chip, and that can be generated, modulated and detected.

The choice of Silicon as the material for integration of these photonic circuits can be ascribed to the following reasons:

- Silicon chip platforms are low-cost and already used for CMOS technology and

ICs, allowing to integrate both photonic and electronic circuits on the same chip.

- Silicon foundries that produce highly controlled Si-wafers already exists, so it is easier to produce devices with less defects i.e. interstitial or surface defects.
- The transparency of Silicon at wavelengths higher than  $1.1\mu m$  makes it perfectly suitable for optical communications.

In spite of every advantage and that many optical devices have been successfully developed in Silicon photonics, the main drawback remains that to full have a Silicon photonic device there is the need of a Laser source, that is unfortunately still missing, due to the physical difficulties mentioned above. Beyond this, one of the most challenging topics is the integrability of Photonics over platforms. In the following sections will be analyzed three types of Integrated Circuits (IC): *Monolithically ICs*, *Heterogeneously ICs* and *Hybrid ICs*.

### 1.3 Monolithically integrated circuits

As it usually happens for the integration of electronic circuits, also photonic circuits are realized with planar geometry, which means that to define structures in both cases there are similar techniques.

Nevertheless, there is a big difference between electronic ICs and Photonic Integrated Circuits (PICs), i.e. in photonics different devices require different physical characteristics. In detail, for passive photonic devices, like wave-guides, transparent materials are required, i.e. materials with a band-gap larger than the energy of the single photon. On the other hand, for active devices like laser sources materials with a band-gap lower or comparable to the energy of the single photon are required, in order to favour light emission.

Therefore, the ultimate goal is to have a monolithic integration: all elements on a single material layer, despite the fact that to integrate all devices on a single chip, with their own required characteristics, represents the main problem in this field.

[4]

Before going ahead with the analysis of monolithic integration it is needed to clarify

one of the most challenging problems concerning Silicon Photonics: while in integrated electronics each signal is managed through voltages and currents, in photonics the situation is different: optical signals are still generated through a bias current, but their shape is more complex since they are plane waves, described by:

$$\vec{E}(\vec{r}, t) = \vec{A}e^{j(\omega t - \vec{\beta}\vec{r} + \phi)} \tag{1.3}$$

In which  $\vec{r}$  is the position vector,  $t$  indicated time dependency,  $\vec{A}$  is the amplitude of the plane wave,  $\omega$  represents the angular frequency,  $\vec{\beta}$  is the propagation vector and  $\phi$  is the phase.

Having optical signals in form of plane waves complicates the integration, since there will be the necessity of a certain number of photonic devices to control each parameter of the equation 1.3. For example, to control and properly change the phase of the plane wave, in certain application there is the necessity to introduce a phase section; this is true also for other parameters.

In spite of every obstacle, great strides have been made since the advent of this new technology as it is depicted in Fig.1.2.

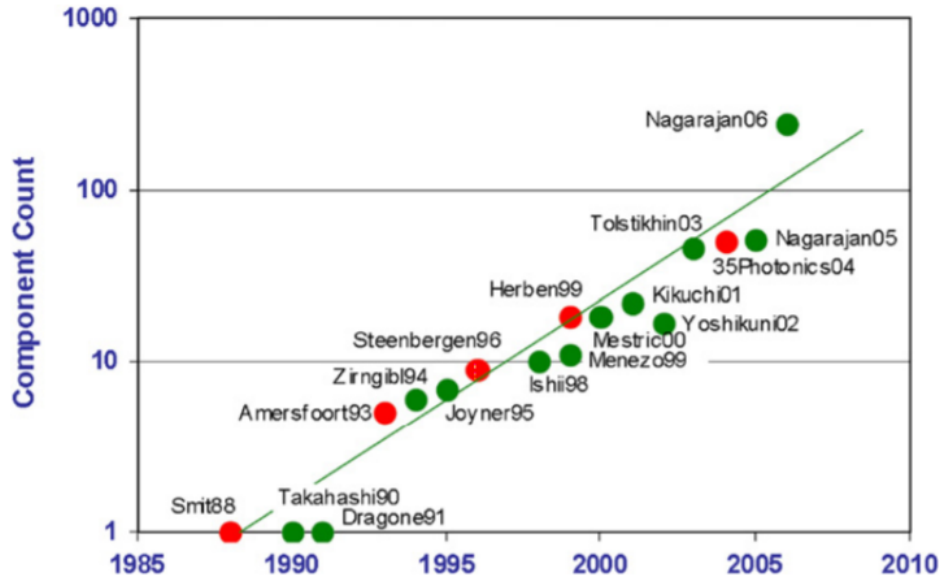


Figure 1.2: Moore's law for photonics [5]

As it can be noticed there is an exponential growth of elements on PICs, very similar

to Moore’s law that governs the integration of components on a single Integrated Circuit.

Another benefits for choosing the monolithical integration for photonic circuits is that this technology allows to reduce two parasitic capacitance [6]:

- the one of the interconnection between optical transceiver electronic and photonic devices on the same die;
- the one between the transceiver chip and package substrate.

The big drawback of this technique is that when some process optimization are needed, these optimizations will for photonic and electronic parts won’t be independent from each other. This represents a big problem, but a good solution could be using old CMOS processes for the fabrication of electronic parts, since they results almost insensitive to variation in fabrication processes for photonic purposes.

For example, since on the same chip coexists both electronic components, i.e. mainly transistors, and photonics, making a fabrication process variation like adding or changing an epitaxial layer of the chip substrate, will be better tolerated by electronic components with a bigger aspect ratio, it means by bigger transistors, which require smaller lithographic precision.

This is in contrast with the necessity of a high lithographic precision, in order to fabricate small photonic devices like ring resonators.

The solution adopted in [6] is called *zero change* and it consists in using technology node of Silicon-On-Insulator CMOS at 45nm and 35nm, which have a ratio  $f_T/f_{max}$  higher than others, in which  $f_T$  is the frequency at which the transistor current gain is unitary and  $f_{max}$  is the frequency at which the transistor power gain is unitary, both of them represent figure of merits for electronics integrated components, at the same time this solution guarantee also photonic performances required with new lithographic processes. It is called zero change since fabrication steps of native CMOS processes are maintained intact.

## 1.4 Heterogeneously integrated circuits

In previous section it has been mentioned that the Silicon Photonic was born, also and above all, because of the convenience given by a great maturity level reached by CMOS technology, so to easily integrate photonic devices on already tested platforms.

Concerning modern microprocessors, in order to overcome scalability limitations, a successful approach is represented by Heterogeneous Integration. It can be a low cost solution, still maintaining high performances also for active photonic devices like Lasers despite all the physical limitations.

This above mentioned method consists in positioning III-V layers, needed for the realization of photonic components, directly on Silicon substrate, which can be accomplished following three approaches: [7]

- The III-V chip is directly bonded on Silicon substrate with coarse alignment and then processed on the Silicon wafer itself. This approach allows to minimize the required area for III-V materials, minimizing also the cost.
- The second approach requires a direct epitaxial growth of III-V compounds using buffer layers to minimize dislocations due to different lattice constants between the grown compound and Silicon substrate. Combining these buffer layers with Quantum Dot lasers maximizes the power output furthermore improving performances. The drawback is that the laser lifetime is still not adequate for most applications.
- The last approach is a combination of the previous mentioned: growing III-V quantum dot material over Silicon and then bonding to Silicon on Insulator substrate. It maintains the benefits of second approach, still having the reduction of area of the first one.

The heterogeneous integration on Silicon platforms goes also beyond III-V compounds, through the use of different materials still able to interact, modulate, detect and amplify light. One of the most used materials is  $LiNbO_3$ , which is already spreading in photonic devices due to its great performances in modulators and light detectors. In particular, its integration over Silicon has been already demonstrated

with good results and performances, despite that it has shown limitations concerning frequency range, reaching only intervals of few GHz.

As mentioned in previous sections, different optical devices require different physical characteristics, leading to a differentiation also for their integration. The whole range of optical components can be divided in three categories: optical interconnections, passive optical components and active optical components.

### 1.4.1 Optical Interconnections

Interconnections represent one of the most important elements in the actual technological scenario, ensuring the overcoming of a big limitation introduced by the Moore's law: as the number of transistors per chip is growing, also the number of interconnections has to grow, still maintaining the power consumption at an acceptable value.

The biggest problem of electrical interconnections is that the information transmission, i.e. number of bits per second, is limited by the aspect ratio of connections, situation not solvable even through shrinking or enlarging the circuit. On the other hand, this doesn't happen with optical interconnections, that, in fact, are quickly replacing the electrical ones in many fields, even tho for on-chip link there still are many limitations, due to few progresses in bandwidth and power consumption.

### 1.4.2 Passive Optical Components

On the other hand, concerning Passive Optical Components, like filters, waveguides, resonators etc., they are largely employed and actually integrated over Silicon platforms thanks to the fact that  $Si$  and  $SiO_2$  combined form a couple of refractive index very steep, allowing the creation of components with strong light confinement.

Moreover, having Silicon as platform guarantees that these devices are transparent in the communication windows, at  $1300nm$  and  $1500nm$ , as it is shown in Figure(1.3). In Figure(1.3) is depicted the relation between the attenuation and wavelength, in which are shown three regions (red, green and blue in the picture), each of them characterised by three different scattering phenomena: Rayleigh scattering, impurity absorption and molecular absorption.

The figure of merit allowing to understand if the integration of passive components

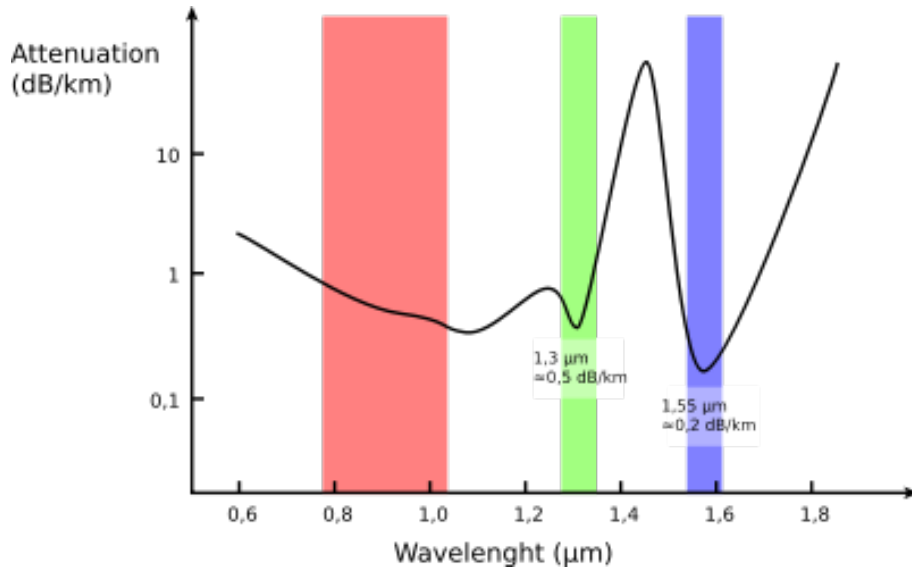


Figure 1.3: Optical transmission windows

if particularly functional is given by the amount of *propagation losses*, in particular, the integration of ring resonators with radii of almost  $1 \mu\text{m}$  has already shown propagation losses lower than  $1\text{dB}/\text{cm}$ .

In the paper [8] it has been demonstrated that Silicon ring resonators show losses up to  $3\text{dB}/\text{m}$  at wavelength of  $1600\text{nm}$ , and also that to reduce furthermore these losses there is the need to use configurations with stronger light confinement.

Another possibility for integrated passive optical devices can be reached through the use of  $\text{Si}_3\text{N}_4$ , a compound easily integrable over Silicon, showing coupling losses -between components and substrate - sufficiently small, also adding the advantage that this compound doesn't show effects like Two Photon Absorption and consequently Free Carrier Absorption.

### 1.4.3 Active Optical Components

About active optical devices, like lasers, research has done many steps forward for heterogeneously integration, in particular for ridge waveguide lasers, fabricated with *InAs* Quantum Dots, directly grown on Silicon substrate, showing already satisfactory results.

In addition to these, also microring lasers integration are showing good results,

that will be analyzed in details in the next chapter.

## 1.5 Hybrid Integrated Circuits

Since the Heterogeneous integration relies on the bonding of III-V dies over Silicon Photonic wafers, one of the main drawback of this technology is that the implementation requires a big amount of area of the wafer, and that it will introduce a high thermal resistance.

In order to overcome these limitations, another technology widely used for the fabrication of light sources is the Hybrid Integration, which, in contrast, relies in the optical connection of components, like III-V lasers and gain sections, to the Silicon Photonic platform. In this situation the variety of III-V devices can be mounted on top of the substrate or butt-coupled to it.

This guarantees to maintain the characteristics and performances of the optical components itself, allowing though to use a Silicon Photonic platform. Obviously the integration introduces some limitation, given by the necessity to have a perfect alignment of the III-V devices with the platform; it can be reached through active alignment, that is an expensive technique, or through the use of micro-lens and prisms, allowing a *sub* –  $\mu m$  precision. [9]

This will be the integration technique used for the fabrication of the Laser analysed and simulated in 3.

## 1.6 Platforms for Silicon Photonics

In previous section of this master thesis work advantages and disadvantages of Silicon Photonic in the current landscape have been listed and analysed , highlighting also aspects related to integrability of Photonic devices (active and passive).

In this section the focus will be moved essentially on platforms for Silicon Photonics, in order to guarantee a better integration, trying also to overcome the problems related to lattice constant mismatches and their electronic and insulation characteristics.

Up to now, the mostly used platforms are:

- Silicon-On-Insulator (SOI);
- Silicon Nitride-on-Silica;
- Indium Phosphide (InP);

These will be analyzed in details below.

### 1.6.1 Silicon-On-Insulator Platform

The SOI wafers are made through the superposition of three layers: a Silicon substrate, an intermediate layer of insulator material, usually Silicon di-oxide ( $SiO_2$ ), and a topper layer of Silicon. This solution results to be very important for Silicon Photonics, not only for its benefits for integrability, but also for the fabrication process that is CMOS compatible.

The French company SOITEC [10] has developed a new technology for the production of SOI wafers through a technique called *Smart Cut*, which presents benefits in terms of cleanliness with respect to conventional bonding. The fabrication process is made starting from two initial Silicon wafers, called wafer A and wafer B. As it

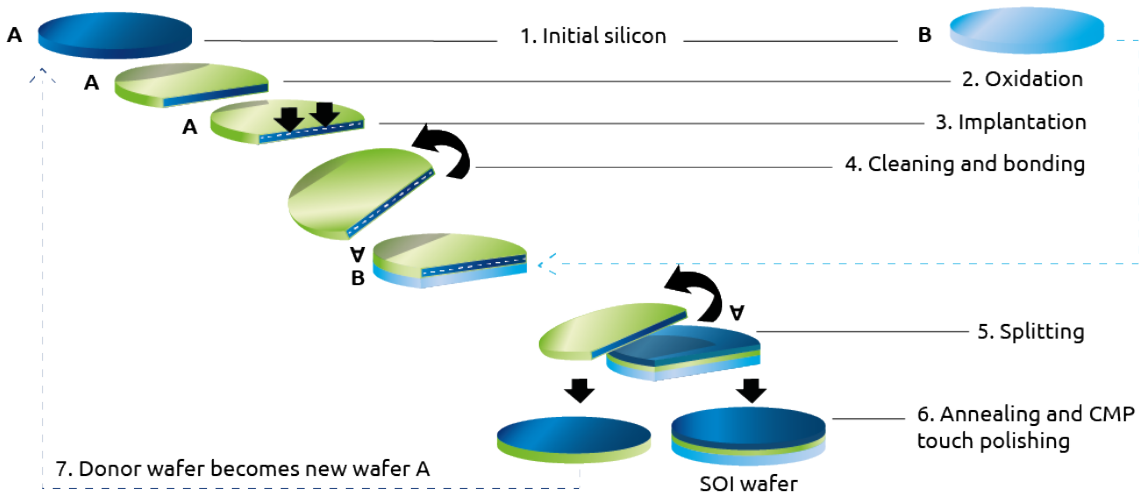


Figure 1.4: Fabrication process of SOI wafer, property of SOITEC.[10]

is depicted in figure 1.4, the wafer A has to undergo several steps:

- Oxidation;

- Implantation of Hydrogen ions ( $H^+$ ), through this step the ions will be positioned a little bit below the surface of Silicon wafer.
- Then wafer A is cleaned, flipped and precisely positioned over the wafer B, which has remained still a simple Silicon wafer without any modification.
- The wafer A is then cut along the line where there was the ion implantation, which weakened Silicon bondings.

At this point, the remaining part of wafer A becomes the new wafer A for another process and the resulting wafer after the annealing results to have an higher quality than with other fabrication processes. Having the insulator sandwiched between two layers of Silicon guarantees the reduction of parasitic capacitance.

For Silicon photonics these platforms are widely used, mainly because they allow to fabricate waveguides with high contrast for refractive index, approximately 2.06, leading to strong light confinement. Indeed, having a high contrast like this, allows to make waveguides with reduced core dimensions, which will have a smaller bending radii ,about  $5\mu m$ , allowing for easy integration for on-chip connections. The transparency range of this platform goes from  $1\mu m$  to values up to  $3.5\mu m$ .

The high contrast of refractive indices leads to an increase of scattering losses, which contributes to increase the value of propagation losses up to 2 dB/cm. Further, the strong light confinement leads to a significant increase in the optical power density, which enables phenomena like Two Photon Absorption and Free Carrier Absorption, increasing the above mentioned losses.

### 1.6.2 SiN-on-Silica Platform

For what concerns platforms in Silicon Nitride, it is considered as example the article [11] in which is presented a platform  $SiN - on - SiO_2$ , called *TriPleX*. It is a very versatile platform, obtained through the alternation of  $SiN$  and  $SiO_2$  layers, in which the transparency range results to be wide enough going from  $0.4\mu m$  to  $2.35\mu m$ .

As previously confirmed for SOI platforms, also in this scenario the production and manufacturing processes are CMOS compatible, guaranteeing low cost production,

making use of a fabrication process called the Low Pressure Chemical Vapour Deposition (LPCVD).

About performances of integrated photonic devices over TriPleX, as already mentioned, one of most important parameters to be taken into account is the ratio between refractive indices, that can allow for strong or weak light confinement; these platforms allow to choose between high and low contrast just by modifying the volumes ratio between different layers, leading also to variations of propagation losses.

It has been demonstrated that with some optimization propagation losses can go down up to  $0.0005\text{dB}/\text{cm}$ , still with bending radii very small, in the order of a few tens of micrometers.

### 1.6.3 InP Platform

Indium phosphide platforms have emerged as a promising solution for silicon photonics due to their high electron mobility, high quality lattice matching and tunable bandgap. They offer a significant advantage over silicon photonics in terms of material quality.

The high electron mobility of InP enables faster device operation than silicon, and its direct bandgap properties allow efficient light emission and absorption. In addition, the lattice match between InP and other III-V materials allows the growth of hetero-structures with reduced dislocation density.

# Chapter 2

## State of the Art

Current state of the art on integrated lasers on silicon photonic platforms results quite vast. It was decided to analyze mainly the work of two of the most prominent research groups in the field of hybrid and heterogeneously integrated lasers: the group headed by Klaus-Jochen Boller, University of Twente, and the group headed by John E. Bowers, University of California, Santa Barbara, mainly because their work shows many similarities with the laser studied in 3.

In the following we review their main works, about the integration of active optical devices, thus lasers, analyzing the characteristics of the proposed works, taking into account the linewidth, tunability, and the degree of complexity for their fabrication and integration on the platform.

### 2.1 John E. Bowers research group

The first paper being analysed is entitled "High power sub-KHz linewidth lasers fully integrated on Silicon", published in 2019. [12] The goal of this research study is to demonstrate the realisation of two ULN (Ultralow Noise) lasers: a fully integrated E-DBR (Distributed Bragg Reflector) laser with a linewidth of approximately  $1\text{KHz}$  and optical output power greater than  $37\text{mW}$ , and also a DBR-ring-assisted (RAE-DBR) laser, with radius of the rings of  $600\mu\text{m}$  and coupling coefficient of 0.04, that can achieve an even smaller linewidth of less than  $500\text{Hz}$ .

ULN lasers are in high demand in various fields and have to fulfil certain requirements to be defined as such: very low RIN (Relative Intensity Noise), narrow and Lorentzian shape linewidth, and very low frequency noise.

In order to meet these requirements, the best solution would be to use a heterogeneous integration approach as it does not have the typical defect of monolithic

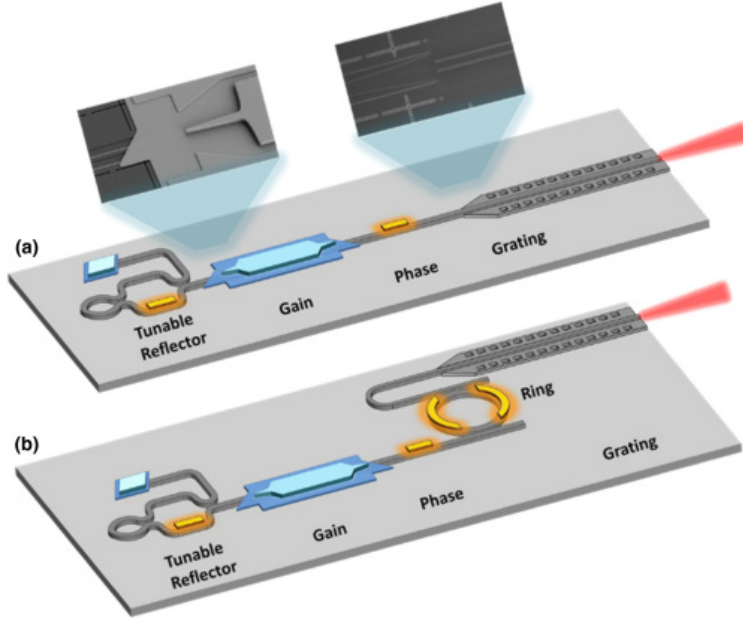


Figure 2.1: E-DBR laser and RAE-DBR laser

integration, namely the great difficulty in scaling the device. In the present article, authors decide to use a III-V on Silicon platform, built with CMOS-compatible technology, with the purpose of exploit the benefits of heterogeneous integration of Silicon Photonics. Over this platform the two different laser configurations are developed, the first a DBR laser with an elongated cavity and the second with also a micro ring resonator to further increase the cavity path, which, as previously mentioned in this thesis, helps to increase photon lifetime, narrowing the linewidth.

In fact, the requirements that lasers must have in order to meet the proposed specifications (very narrow linewidth), are mainly two: very low propagation losses  $\alpha_p$ , and fairly weak perturbations, i.e. low  $\mathbf{k}$ . The authors decide to set a target for the two main parameters:  $kL \leq 1$  and  $\alpha_p < 0.2dB/cm$

Both proposed lasers were built following the same integration strategy, with the difference that ring resonators were added to one. In particular, both are constructed with the following building blocks:

- Gain section: is a section made of InAlGaAs-on-Silicon multiple quantum well, with a length of 2.5mm.
- Phase control section: is a portion of the circuit that can be tuned to ensure

alignment between the laser mode and the Bragg grating reflection peak. This tuning is thermally induced, through the overheating of a metal resistor placed above that portion of the circuit.

- Back mirror: the back mirror of the cavity is realised with of a tunable reflector made from an MZI (Mach-Zender Interferometer) followed by a loop mirror.

The characterization of both devices was carried out following a common scheme and is, in the article, divided into Reflector Characterization and Laser Characterization.

About the first topic, the DBR of both lasers was characterised by reverse biasing the gain section, which behaves like a photodiode and generates a photogenerated current  $I_{PD}$ . In the case of the E-DBR, this photogenerated current provides a direct measure of the transmission spectrum of the grating, therefore the reflection spectrum is calculated from this value. This characterization is carried on considering three values for grating strength  $kL$ : 0.375, 0.75, 3. It is demonstrated that increasing this number, also bandwidth and reflectivity increase.

In contrast, when characterizing the ring-assisted E-DBR laser, the generated photocurrent  $I_{PD}$  provides a measure for both the grating transmission spectrum and the ring transmission spectrum at the drop port, and it is demonstrated in the article that the grating reflectivity reaches a level of approximately 80%, giving the target  $kL = 1$ .

The second topic is the Laser characterization, for which both lasers are characterized with a temperature-controlled cycle, at room temperature. For the E-DBR the LIV (Light Current Voltage) characteristic, considering grating long 15mm, and the grating strength fixed at  $kL = 0.375$  is: With threshold current  $I_{TH} = 50mA$  and maximum output power  $P_{out} = 37mW$ . As it is depicted in Figure(2.2), the black curve shows a crimping, this is due to the fact that in this configuration, as temperature increases in gain section, as a consequence of the increase of current, the mode-hopping phenomenon arise, so the lasing mode is detuned from the reflection peak and it entails a power output reduction. This effect is mitigated by the phase section, which is able to re-tune the lasing mode to the reflection peak.

About the second configuration of the laser, which is equipped with the ring resonator, the LI characteristic is shown in Figure(2.3).

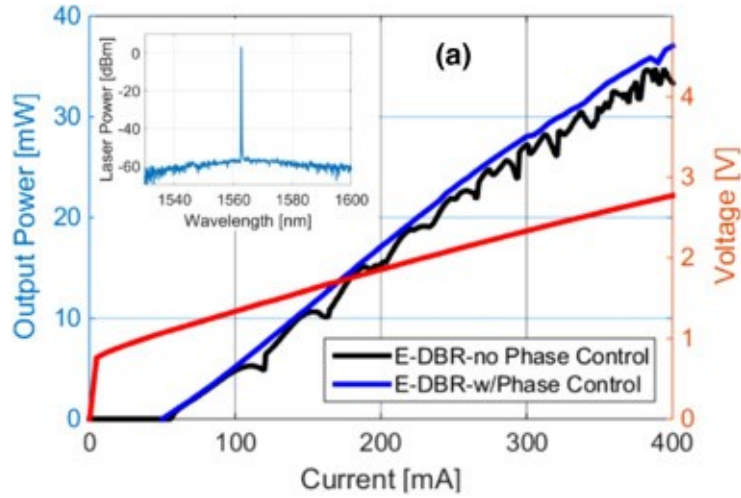


Figure 2.2: Light-Current-Voltage characteristic E-DBR.

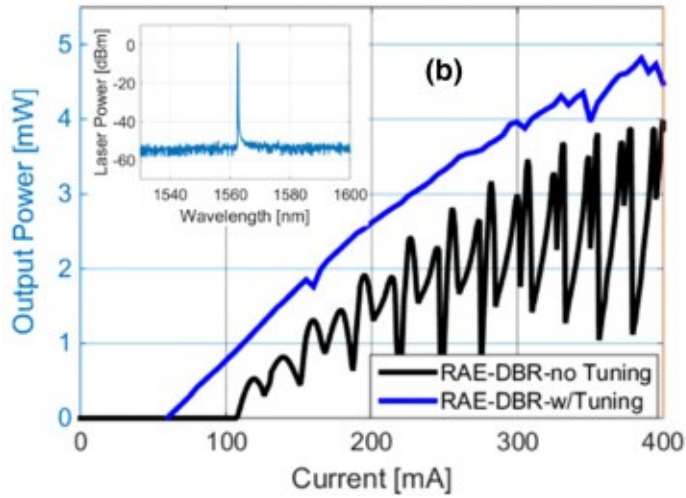


Figure 2.3: Light-Current characteristic RAE-DBR.

Since the FWHM of the ring resonator reflectivity is much smaller with respect to the grating, the ring has to be tuned to the Bragg grating characteristic wavelength. It can be noticed that in this case the threshold current is  $I_{TH} = 60\text{mA}$  and the maximum output power is  $P_{out} = 4.8\text{mW}$ , it is a value far from the one of E-DBR, that was  $P_{out} = 37\text{mW}$  mainly due to the longer path that light has to travel, so propagation losses are higher.

Also here, increasing the current leads to mode hopping, and indeed the purpose

of the ring is also to help tune lasing mode at the reflection peak. If the laser is operating near a mode hop -without tuning- there will be a multi-mode behaviour, with a sudden reduction of output power at the lasing wavelength.

In order to better understand this situation is reported the Figure(2.4), from which it can be seen that when the laser is operating in a region near mode-hop, there is a drop in power output, since other longitudinal modes are competing to the lasing one.

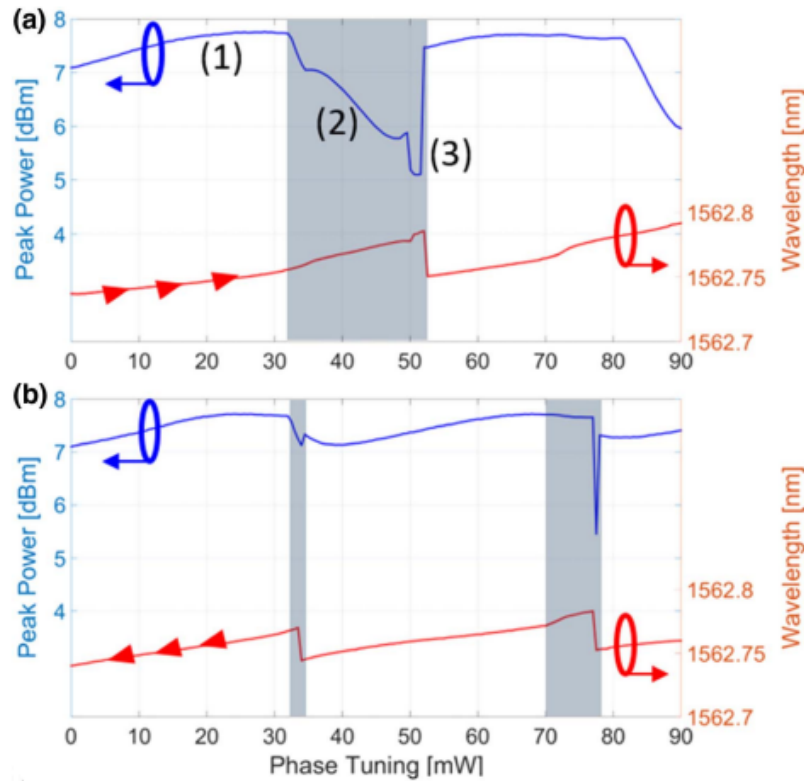


Figure 2.4: Multi-mode regions.

Furthermore, in this article is also analysed spectral linewidth, showing that in both configurations the linewidth results to be very narrow, in particular,  $1.1kHz$  for E-DBR and  $500Hz$  for the ring-assisted E-DBR, the difference is given by the less sensitivity to grating strength by the second laser configuration, reaching a lower value.

In conclusion, authors demonstrate that both lasers reach high performances in terms of output power, and linewidth, still with a low degree of complexity, i.e.

using one microring at most, indeed in the ring-assisted case it is used only one ring resonator.

Another paper taken into consideration by this research group is "Ring-Resonator based widely-tunable narrow-linewidth Si/InP integrated Lasers" [13], published in 2020.

In this article two lasers are demonstrated, identified from now on as I and II generation laser, both heterogeneously integrated over Si/InP platforms and both using ring resonators as one of the building blocks of the resonant cavity.

The employment of Ring Resonators is of primary importance not only as a tuning mechanism, but also for linewidth reduction, and it will be analyzed further.

In the I laser generation, authors decided to use classic rib waveguides made of Silicon, while in the II laser generation, there are low-loss Silicon waveguides that allow to fabricate ring resonators of higher quality, i.e. with lower propagation losses and with lower bending radii, allowing for smaller devices.

Also in this case the structure of these two integrated devices is characterized by the use of building blocks, as it is shown in Figure(2.5), in which are depicted three rings as the most general case, while in the I generation the building block is made of only two ring resonators, shown in Figure(2.8) and in the II generation is made of three rings, as it is in Figure(2.9). That are analyzed below:

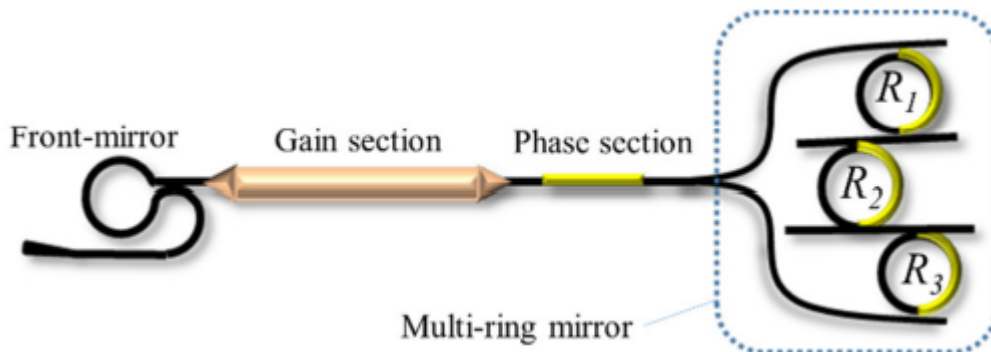


Figure 2.5: Structure of multiring laser.

- Front Mirror: it is employed a *Sagnac Loop Mirror* as light output of the laser, since it is fabricated to have low reflectivity on the facet.
- Gain Section: it is fabricated using a Silicon rib waveguide over which is placed

a III-V material, in its completeness it constitutes an optical amplifier.

- Phase Section: also in this case, as in [12] this section is made of a metallic component thermally tunable.
- Resonant Mirror: this section is made of multi-ring resonators equipped each of them with a self thermal phase tuner, in order to guarantee the linewidth tuning.

The different ring resonators show different values of radii, each of them placed in add-drop configuration with a cascading mirror loop: in this configuration they form a Vernier filter.

The Free Spectral Range (FSR) of Vernier filter is calculated as:

$$FSR_v = \frac{FSR_1 \cdot FSR_2}{|FSR_1 - FSR_2|} \quad (2.1)$$

In which:

$$FSR_{1,2} = \frac{\lambda^2}{2\pi r_{1,2} n_g} \quad (2.2)$$

The purpose of calculating the Free Spectral Range of the Vernier filter is that this quantity determines the range of tunability of the entire laser (both for I and II generation) while the resonance tuning of each ring is determined by the phase section.

Both lasers are modeled through a three-block scheme, made of a gain section, a passive section and ring mirror. Successively, this scheme is simplified in a model in which the last two sections are shrunk in an effective reflection coefficient, as it is shown in Figure(2.6)

This coefficient is given by the following formula:

$$r_{eff}(\omega) = t_{transitions}^2(\omega) \cdot t_{passive}^2(\omega) \cdot r_{mirror}(\omega) \quad (2.3)$$

In which  $t_{transitions}^2(\omega)$  is an attenuation term inserted in this equation to take into account losses that happens through the path between the active region and passive region of devices, it is calculated numerically and it is almost  $-1dB$ .

The coefficient  $t_{passive}^2(\omega)$  represents the transfer function of the lasers, considering

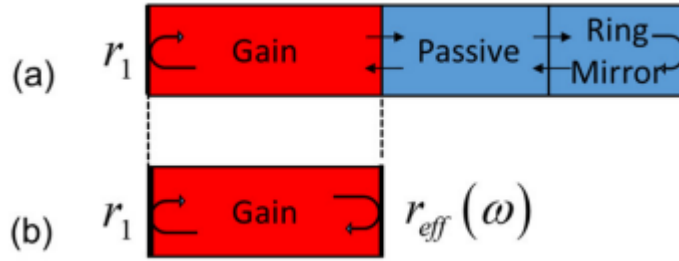


Figure 2.6: Three-block scheme with simplification.

the total length of the cavity, the propagation losses of electric field through the waveguide and the propagation constant of the waveguide.

The last term,  $r_{mirror}(\omega)$ , represents the reflection coefficient accounting for the multiple ring resonators.

In order to determine the laser's linewidth authors have decided to re-use a formalism demonstrated by [14] and [15], in which the frequency dependence in phase and reflectivity is considered, concluding that the effective lasers' linewidth is equal to the Schawlow-Tones linewidth of a single Fabry-Perot laser weighted by a factor  $F^2$ ,  $F = 1 + A + B$ , for which the linewidth becomes:

$$\Delta\nu = \frac{\Delta\nu_0}{F^2} = \frac{\Delta\nu_0}{(1 + A + B)^2} \quad (2.4)$$

In which terms A and B are defined as:

$$A = \frac{1}{\tau_0} \text{Re} \left[ j \frac{d \ln(r_{eff}(\omega))}{d\omega} \right] = \frac{1}{\tau_0} \frac{d\phi_{eff}}{d\omega} \quad (2.5)$$

$$B = -\frac{\alpha_H}{\tau_0} \text{Im} \left[ j \frac{d \ln(r_{eff}(\omega))}{d\omega} \right] = \frac{\alpha_H}{\tau_0} \frac{d \ln |r_{eff}(\omega)|}{d\omega} \quad (2.6)$$

In which both equations shows the term  $\tau_0$  that represents the photon round trip time in the active region,  $r_{eff}$  is the effective reflectivity,  $\alpha_H$  is the linewidth enhancement factor and  $\phi_{eff}$  indicates the phase dependence.

The A factor indicates a phase variation over the round-trip. When A increases, it means that increases also the length of passive section of the cavity, so it will be higher also the occupied volume from photons. This means that the optical confinement factor will decrease in the length direction.

Having a confinement factor sufficiently low, leads to have also a lower noise spectrum since there will be a smaller spontaneous emission rate in the lasing mode. This means that by manipulating the factor A opportunely it can be possible to reduce the linewidth.

Otherwise, the coefficient B stands for the intensity of a phenomenon called Detune Loading, characterised by the linewidth enhancement factor  $\alpha_H$ . This means that it can happen an enlargement or a shrinking of the linewidth depending on the factor  $\alpha_H$ . It needs to be pointed out that in the case of extended cavity lasers B is directly proportional to  $\alpha_H$ , while for a solitary laser B is proportional to  $(1 + \alpha_H^2)$ , this indicates a less strict dependencies from this phenomenon. In order to better understand the Detuned Loading it is reported Figure(2.7) which shows a situation in which the mirror reflectivity is a function of the optical frequency. When the lasing frequency is increasing up to the peak, the reflectivity increases too, leading to an increase also of the cavity photon density. At the growth of photon density the carrier density in the cavity decreases, so it does also the lasing frequency. This is a negative feedback loop that is necessary to stabilise the linewidth. On the contrary, at the negative slope of the curve in Figure, there is the creation of a positive feedback loop, which, instead, let the linewidth spread.

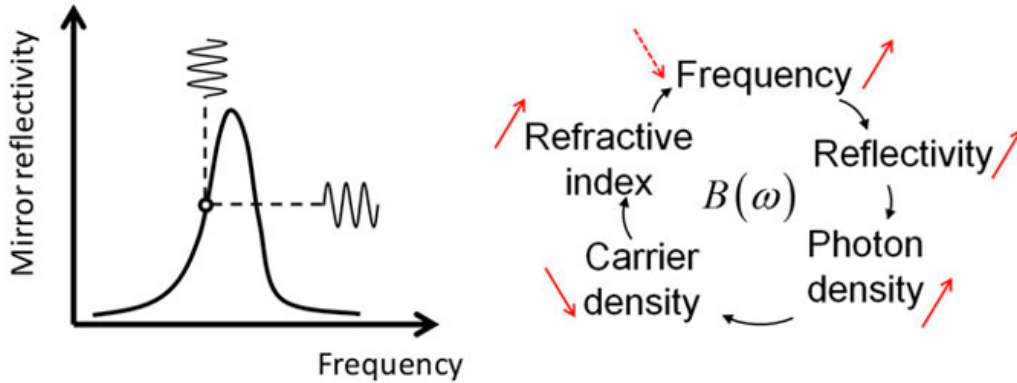


Figure 2.7: Detuned Loading effect [16]

Concerning the architecture and the structure of both lasers, both generations are

made with the same productive processes, with the difference that in the second case are exploited ultra low loss waveguides.

About the first generation of laser, it is fabricated using rib waveguides etched 231 nm out of 500 nm, showing losses of about 1 dB/cm, and for the structure of the two ring resonators the choice was for radii higher than  $60\mu m$ , such that bending losses were negligible.

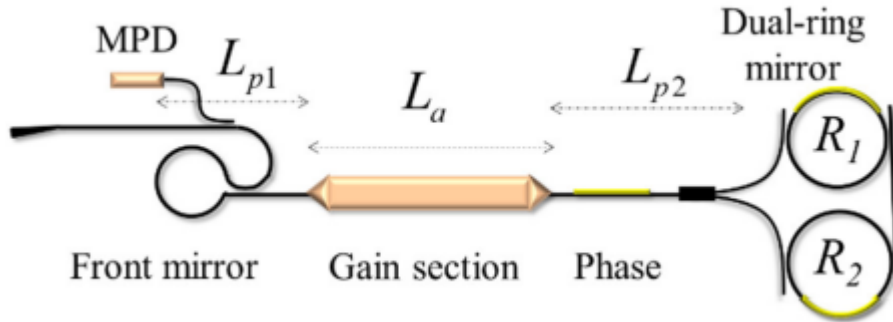


Figure 2.8: Structure of the first generation of laser.

In such conditions, the laser shows a linewidth at the ring resonant frequency of almost 5kHz, but with proper tuning it could be reduced up to 2 kHz, exploiting the effect of detune loading.

This kind of laser was characterised in a temperature controlled environment, set at  $20^{\circ}C$ , with at the output of the laser an opto-isolator, able to eliminate back reflections that enters back at the interface. With this particular setting, the device shows a threshold current  $I_{TH} = 30mA$ , then is biased with a current  $I_{bias} = 120mA$ , four times higher than the threshold, proving to have a stable single mode behaviour for 40 nm of wavelength spectrum. The Lorentzian linewidth is calculated starting from the measurement of the frequency noise spectrum, having as result almost 2kHz, that corresponds to the theoretical results.

As previously mentioned, in the second generation of the laser ultra low loss Silicon waveguides have been used, still rib waveguides but etched 56nm out of 500nm, moreover there is also another improvement, and it is the use of three ring resonators instead of two. The combination of these two configurations lead to a further narrowing of the linewidth, up to hundreds of Hertz.

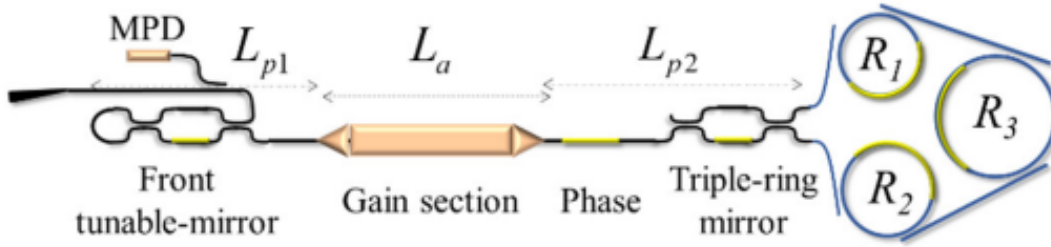


Figure 2.9: Structure of the second generation of laser.

In this case, the structure results to be quite different with respect to the previous generation, still maintaining though the same building blocks. In particular, the front mirror is made of a tunable Mach-Zehnder Interferometer (MZI) directional coupler; the Gain Section in its structure has been maintained as it was, increasing only the length to 2.5mm. The mostly changed structure is the Multiring Mirror, in which there are three ring resonators in add-drop configuration, which show losses of almost 0.16dB/cm and minimum bending radii of  $600\mu m$ , larger than the previous analysed structure.

Having bending radii larger than the previous structure means having a reduction of ring FSR, such that if before there was the need of two rings to achieve the wanted SMSR, now at least three are needed. These three rings have been fabricated with three different radii, calculated with a proper algorithm, such that they result to be able to provide a tuning range of 120 nm. With this structure is achieved the SMSR higher than 8 dB.

Concerning the linewidth, the theoretical analysis has been carried on through the same approach of the previous generation, reaching a value for  $\Delta\nu$  lower than 100 Hz, considering 10mW of output power, value that, though, is not possible to achieve in this configuration, since it is higher of the possible output power value.

The laser characterisation is made with the same setting, environmental and electric, of the previous case, showing a threshold current  $I_{TH} = 100mA$ . To carry on the simulations the device is biased with  $I_{bias} = 300mA$ , three times higher than the threshold, having as result a single mode behaviour tunable over a frequency span of 110 nm, and a Side Mode Suppression Ratio higher than 40 dB for each mode.

The experimental results for the linewidth have been generated through a commercial phase noise measurement system, demonstrating  $\Delta\nu$  lower than 220 Hz, that is an incredibly low value for this kind of systems.

## 2.2 Klaus J. Boller research group

About the group headed by K.J.Boller, the first article to be analysed is "Linewidth narrowing via low-loss dielectric waveguide feedback circuits in hybrid integrated frequency comb lasers" published in 2019. [17]

The goal of this article is to demonstrate an integrated hybrid  $InP - Si_3N_4$  waveguide laser that is able to generate frequency combs at a wavelength of around  $1.5\mu m$ , showing narrow linewidth of  $34KHz$ . An effective way to reach this purpose is to increase the effective cavity length to consequently increase photon lifetime.

Since the goal of this paper is to obtain a very narrow linewidth in the order of few KHz, authors have decided to use micro-ring resonators integrated in the structure of the device. About this achievement, a challenging problem is highlighted by the authors, it is the increase of photon lifetime extending effective cavity length using Silicon waveguides, which shows a band-gap that is not sufficiently large, of about  $1.1eV$ . This lead to have, in addition to the usual linear propagation losses, also non-linear losses due to Two Photon Absorption phenomenon, that play an important role in the broadening of emission linewidth.

Exactly for this reason, this study has been done considering a structure with dielectric waveguides ( $Si_3N_4/SiO_2$ ), which guarantee band-gaps of  $5eV$  and  $8eV$ , showing extremely low propagation losses.

The proposed laser structure is depicted in Figure(2.10), this configuration is very similar to the one that will be considered 3.

Two fundamental blocks mostly describe it, physically separated from each other: RSOA, Reflective Semiconductor Optical Amplifier made of  $InP$  and feedback chip made of  $Si_3N_4$ . In the feedback chip are integrated two micro-ring resonators, which have slightly different radii, positioned there to work as feedback mirrors and tunable element.

The working principle of this device is that light is generated inside of the RSOA,

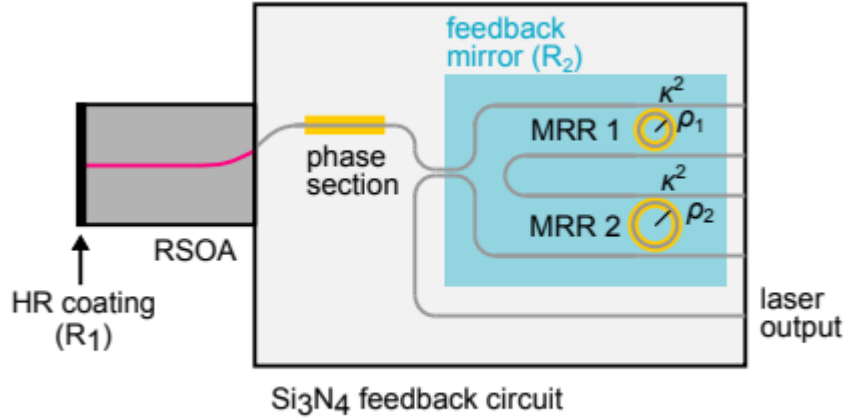


Figure 2.10: Structure of hybrid integrated laser.

then at the interface between RSOA and feedback chip both waveguides are positioned at an angle such that interface reflections can be minimised.

As it is shown in Figure (2.10), when light enters is the feedback circuit, it follows a path along which there are the Phase Section and the two micro-rings. The Phase Section is a thermally-tunable element that is able to optimise the tuning of longitudinal modes of the cavity through changes in thermal coefficient of the material. Beyond the goal of reducing the linewidth, the two micro-ring resonators are used in a configuration such that they form a Vernier filter, which is not only needed to further narrow the linewidth, but is also able to induce the generation of a multimodal comb emission spectrum.

The effective cavity length is the sum of two factors: the geometrical length of RSOA,  $L_1 = 700\mu m$  and the length of  $Si_3N_4$  feedback circuit  $L_2 = 1.6cm$ , these are weighted by refractive indices of materials that compose them:

$$L_{CAV} = 2(n_1L_1 + n_2L_2) \approx 6cm \quad (2.7)$$

Where  $n_1 = 3.6$  and  $n_2 = 1.715$ .

In this situation, the Vernier effect, as previously mentioned, is exploited with the purpose of induce the multi frequency comb generation. This purpose is often reached through setting the spectral position of the two lasing modes placed

symmetrically around the filter transmission peak.

In this paper it is experimentally demonstrated that equidistantly mode-spaced frequency comb spectra can be generated if the two lateral modes receive the equal amount of feedback, this can be reached through a proper tuning of the phase section.

The proposed device is characterised using an external extended-cavity laser as reference, with an Optical Spectrum Analyzer and an Electrical Spectrum Analyzer to inspect results. The laser shows a single mode behaviour when the phase section is tuned such that the lasing mode coincides with the transmission peak of the Vernier filter, with a Side Mode Suppression Ratio (SMSR) of minimum 50dB.

The optical power output is higher than  $10mW$ , value reached considering a bias current  $I_{bias} = 220mA$  and a threshold current of  $I_{TH} = 12mA$ .

When the tuning of the phase section is properly modified, as it is mentioned before, two longitudinal modes receive the same optical feedback and a multi-mode frequency comb is obtained.

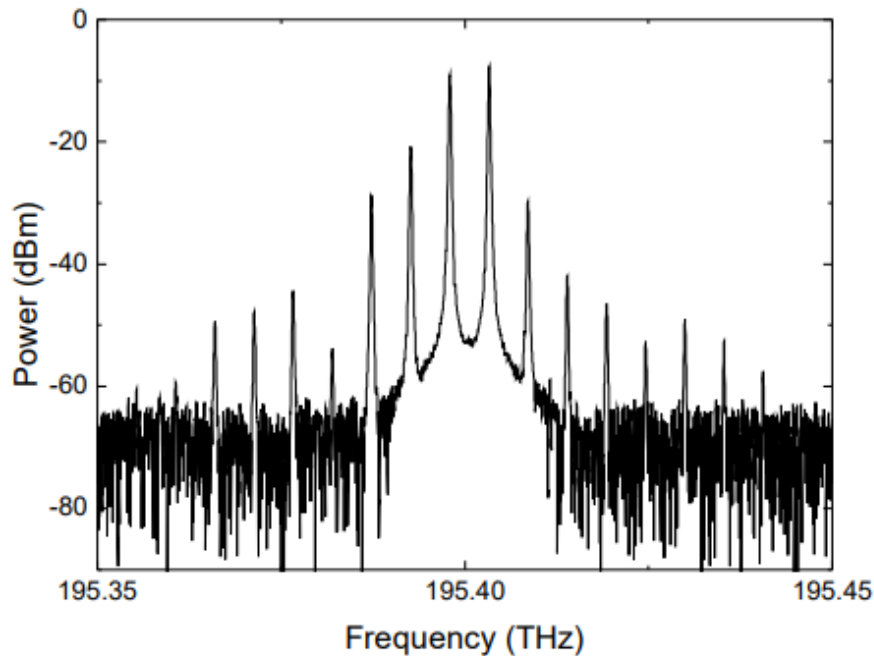


Figure 2.11: Frequency comb spectrum.

In Figure (2.11) it is depicted this particular behaviour, showing that there is the generation of 17 separate and equidistant spectral lines identified from the tuning of micro-ring resonators, which, however, show a decreasing intensity as they get closer to spectrum edges. This situation could be solved through micro-ring resonators used as filter with less steep band edges.

In conclusion, authors of this paper have demonstrated that using an heterogeneously integrated III-V laser, with two micro-rings to extend the cavity, it is possible to obtain a frequency comb with lines spaced of  $5.5GHz$ , and the future goal to increase the spectral bandwidth and reducing linewidth, down to the sub 100 Hz range.

The next paper of this research group is "Hybrid integrated  $InP - Si_3N_4$ " diode laser with a 40Hz intrinsic linewidth, [18] published in 2020.

The author's purpose is to demonstrate an integrated laser which shows an extremely narrow linewidth. In order to achieve it, the laser cavity length needs to be extended to favour longer photon lifetime, and the most effective way is using micro-ring resonators, which can be fabricated using  $Si/SiO_2/SiON/Si_3N_4$  waveguides.

Among these materials, Silicon is the one of easiest integration, showing, though, not enough benefits in reducing the linewidth, due to losses for non-linear phenomena. For this reason, in this paper, are exploited  $Si_3N_4$  waveguides, for which phenomena like Two Photon Absorption are not expected.

These waveguides are coupled to a  $InP$  gain section, in order to provide the wanted linewidth.

In Figure(2.12) is depicted the proposed device scheme, in which is possible to notice that the cavity length has been increased with two different methods:

- Physical increment: through a 33mm long spiral;
- Optical increment: through three coupled ring resonators with a Sagnac loop mirror. In this configuration authors ensured a double trip through the ring's path.

In order to reach the optimum condition to get a narrowing in linewidth, there are three mechanisms that contribute:

- Increasing photon lifetime already in a single round-trip thanks to cavity elongation exploiting low loss waveguides.

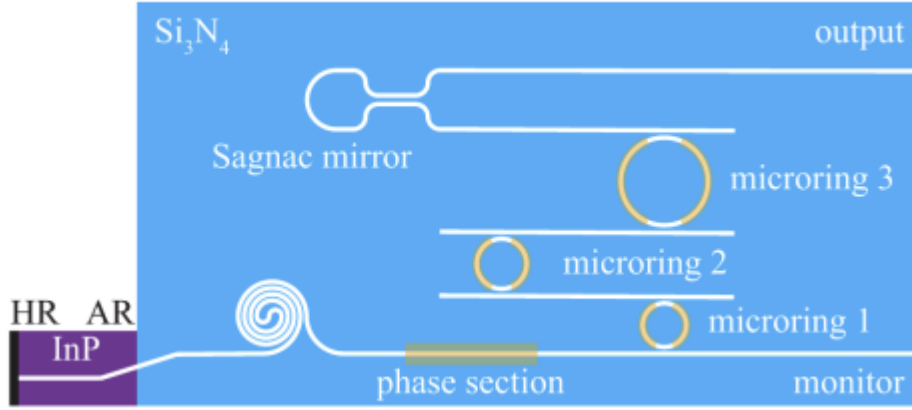


Figure 2.12: Structure of hybrid integrated laser.

- Reducing mode hopping taking advantage of low propagation losses, that allow to a sharp filtering of the single mode output, further reducing the linewidth.
- Using  $Si_3N_4$  waveguides, since this compound shows a large Band Gap to overcome non-linear losses.

Using these mechanisms the linewidth can be narrowed at the power output increase. Respecting all these constriction, the photon lifetime is modelled as:

$$\frac{1}{\tau_p} = \frac{1}{L_g + L_f} (\alpha_i v_{g,i} L_g + \alpha_f v_{g,f} L_f - \frac{1}{2} \langle v_g \rangle \ln(R_b R_s)) \quad (2.8)$$

In which,  $L_g$  is the gain section,  $L_f$  is the feedback arm length,  $\alpha_i$  are the intrinsic losses,  $\alpha_f$  the propagation losses through the feedback arm and  $R_b$ ,  $R_s$  the end mirrors reflectance.

It has been experimentally proved that if the feedback arm length is much more shorter than the gain section length, than the photon lifetime does not change, so in this case the equation can be simplified, becoming  $L_f$  and  $\alpha_f$  independent.

Otherwise, if the feedback length is increased of almost three magnitude's degree (in mm), the propagation losses start to be significant and then dominates, leading to a saturation of the value of photon lifetime, as it is shown in Figure(2.13).

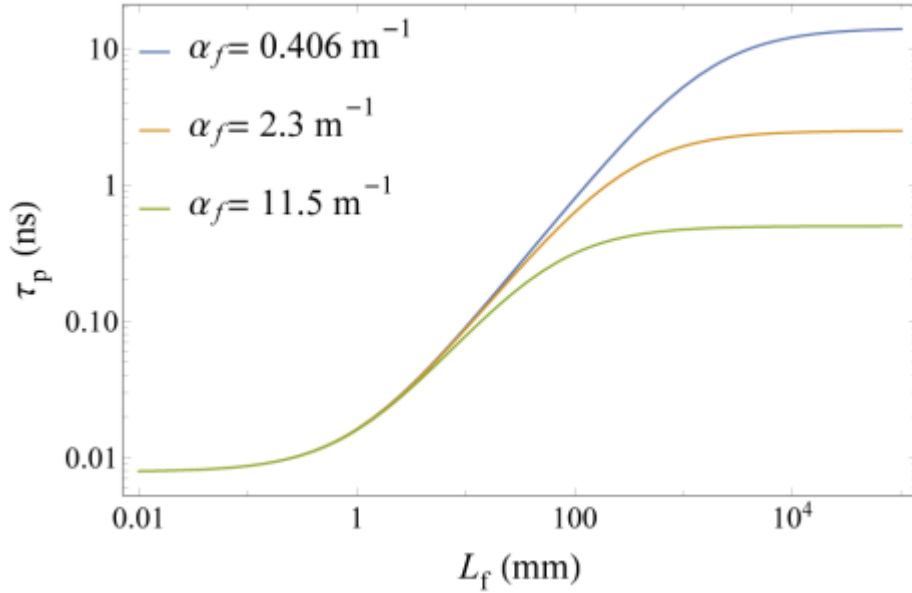


Figure 2.13: Photon lifetime.

Also in this study, as it was in [13] the linewidth is modelled starting from Schawlow-Townes linewidth of a single Fabry-Perot laser, weighted by the factor  $F$ :

$$\Delta\nu \propto \frac{1 + \alpha_H^2}{F^2} \quad (2.9)$$

In which,  $F = 1 + A + B$ .

As previously mentioned, the proposed device is made of two blocks physically separated, with two different purposes. The *InP* gain section consists of a reflective back facet and an anti-reflection coating on the front facet, in order to avoid back reflections in the amplifier *Si<sub>3</sub>N<sub>4</sub>* section.

The technology that has been chosen for the *Si<sub>3</sub>N<sub>4</sub>* circuit is the double strip geometry for waveguides, meaning two cores made of *Si<sub>3</sub>N<sub>4</sub>* with dimensions  $1.2\mu\text{m} \times 170\text{nm}$  in *SiO<sub>2</sub>* cladding. Having this geometry allows to create tight guiding, with low bending losses, almost negligible, optimal condition to create rings with very small radii, of few  $\mu\text{m}$ , and propagation losses of almost  $\alpha_f = 0.1\text{dB/cm}$ .

The particular configuration of this laser cavity, elongated through the spiral and the three rings, led to a round-trip optical length of 74 cm, extending the photon

lifetime of 1 ns.

Two of the three ring resonators are placed in Vernier filter configuration, with slightly different radii:  $r_1 = 99\mu m$  and  $r_2 = 102\mu m$ , while the third one is placed to provide finer spectral filtering, with a wider radius  $r_3 = 1485\mu m$ , the resulting FWHM is 450 MHz.

These three rings are then coupled with the Sagnac loop mirror, and in order to maintain a fixed reflectivity a tunable Mach-Zehnder interferometer is inserted.

Experimental results are obtained, showing a threshold current  $I_{TH} = 42mA$  and a power output  $P_{out} = 23mW$ , obtained with a bias current of  $I_{bias} = 320mA$  considering a wavelength of  $\lambda = 1561nm$ . The measured spectrum is obtained and depicted in Figure(2.14), showing a Side Mode Suppression Ratio (SMSR) of 62dB.

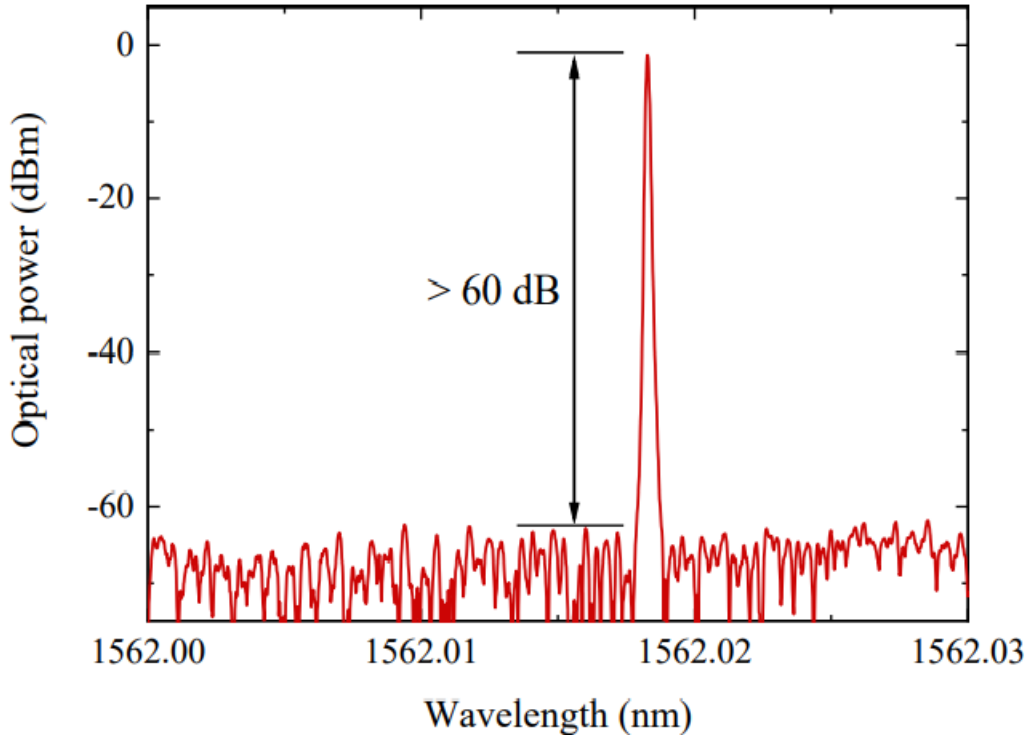


Figure 2.14: Output spectrum.

In conclusion, this paper show an alternative structure for hybrid integrated laser, which is widely tunable and with the required narrowing of the linewidth.

## 2.3 Comparison

In this section are summarised the most important parameters needed for a fully performing tunable laser with a sufficiently small linewidth. Are taken as example the four papers presented, considering only the best trade-off for each research group. In fact, are summarised parameters of [13] and [18] in the following table:

PARAMETER	BOWERS	BOLLER
Linewidth ( $\Delta\nu$ )	220 Hz	40 Hz
Range of Tunability (in frequency)	120 nm	74 nm
Propagation Losses ( $\alpha$ )	0.16 dB/cm	0.1 dB/cm
Degree of Complexity (number of rings)	3	3

# Chapter 3

## Simulations

The principal aim of this master thesis is the analysis of a Silicon Photonics application: design and implementation of a hybrid laser source. This has the purpose to be applicable in a large variety of fields, from optical transceiver for communication links, to sensing and eventually *LIDAR* applications.

While the papers in previous chapters mainly focused on the linewidth narrowing, here we develop and investigate in more details the dynamics of hybrid lasers through a suitable model.

### 3.1 Structure

The structure of the device under exam has been proposed by [19]. This laser has been hybrid integrated, allowing to reap the benefits mentioned in 1.4.

In details, in this case a laser fabricated with two separated sections has been used i.e. a III-V gain section and a Silicon photonics circuit, exploiting micro-ring resonators as narrow band filter.

The proposed structure is depicted in Figure(3.1)

The left section is a commercial Multi Quantum-Well Reflective Semiconductor Optical Amplifier, *RSOA*, fabricated using a III-V compound. It presents two facets, the left one is covered with a layer that allows High Reflectivity (HR), while the right one is covered with Anti-Reflection coating, in order to favour the light path through the interface in the direction of the other section.

The other section of the proposed device is a reflective mirror based on a  $Si_3N_4$  platform, which aims to be the external cavity of the laser, exploiting High-Q ring resonators properties. In fact, the ring's reflectivity results to be dispersive both in amplitude and phase, i.e. varies with frequency, allowing to form a very sharp frequency filter, with FWHM of few GHz.

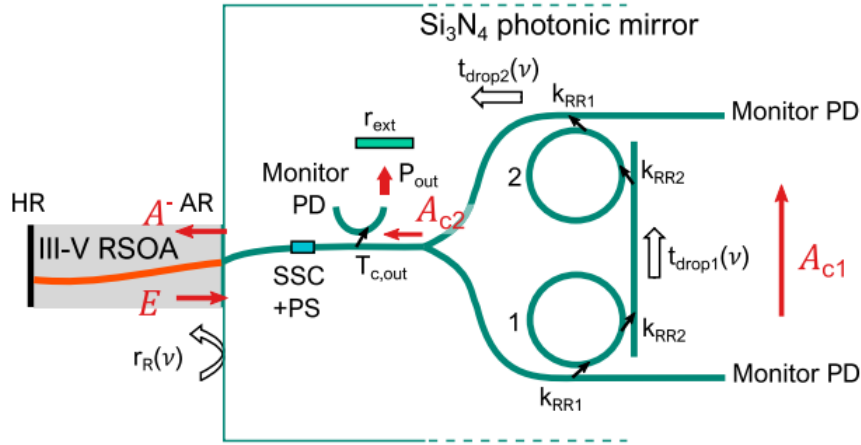


Figure 3.1: Hybrid laser structure.

In this case the two rings have radii of about  $100 \mu\text{m}$ , chosen to maximize the tuning, forming a Vernier filter, while minimizing the overlap between resonance peaks. The power coupling coefficients between the rings and the straight waveguides are chosen equals to each other in order to maximize the reflection in the critical coupling regime.

In this effective mirror section the field follows a precise path: the electric field  $E$  from the RSOA enters in the  $\text{Si}_3\text{N}_4$  mirror section through the anti-reflection facet, passing through the straight waveguide where is placed the Phase section. After that, the field proceeds in the direction of the Y-junction, with the waveguide coupled to the first ring, through the power coupling coefficient  $k_{RR1}$ , and the field is collected at the drop port,  $A_{c1}$ , which re-enters in the second ring.

At this point, the field at the drop port of the second ring is collected,  $A_{c2}$ , then proceeding backwards on the upper part of the straight waveguide entering in the RSOA.

As it is shown in Figure(3.1), the output power  $P_{out}$  is collected with means of a output coupler placed behind the straight waveguide, as it is shown in Figure.

## 3.2 Mathematical model

The set of equations [19] that describe the behavior of the proposed device are:

$$E(t) = \frac{e^{j(\omega_s - \omega_0)\tau_{IN}} \cdot e^{\frac{1}{\tau_{IN}} \int_{t-\tau_{IN}}^t L(1+j\alpha\frac{\omega_s}{\omega_0})g_N \ln(\frac{N(t)}{N_S})d\bar{t}}}{r_R(\omega_S)} A^-(t - \tau_{IN}) + F(t) \quad (3.1)$$

Which represents the slowly varying envelope of the Electric field at the AR-coated facet of the RSOA entering the SiPh circuit. Here  $F(t)$  is a term introduced to take into account the spontaneous emission noise, and  $A^-(t - \tau_{IN})$  is the envelope of the electric field exiting the SiPh circuit:

$$A^-(t - \tau_{IN}) = t_{SSC} \sqrt{1 - T_{c,out}} e^{-j\Delta\phi/2} A_{c2}(t - \tau_{IN} - \frac{\tau_{IN,SiN}}{2}) + t_{SSC}^2 T_{c,out} r_{ext} e^{-j\phi_{ext}} E(t - \tau_{IN} - \tau_{ext}) \quad (3.2)$$

Considering that in this work the external reflection is not taken into account, the second term can be neglected.

$$\frac{dA_{c1}(t)}{dt} = \gamma_{c1} t_{SSC} \sqrt{1 - T_{c,out}} E(t - \tau_{IN,SiN}/2) e^{-j\Delta\phi/2} - \gamma_{t1} A_{c1}(t) \quad (3.3)$$

This is the differential equation that describes the envelope of the electric field collected at the drop port of the first ring resonator.

$$\frac{dA_{c2}(t)}{dt} = \gamma_{c2} A_{c1}(t) - \gamma_{t2} A_{c2}(t) \quad (3.4)$$

Similarly to Eq.(3.3) this equation stands for the envelope of the electric field collected at the drop port of the second ring resonator.

$$\frac{dN(t)}{dt} = \frac{\eta_i I}{qV} - \frac{N(t)}{\tau_N} - v_g g_N \ln(\frac{N(t)}{N_0}) \sigma \frac{|E(t)|^2}{V} \quad (3.5)$$

3.5 is the equation that describe the carrier variation through time, showing two phenomena, *Generation*, given by the first term, and *Recombination*, described by the latter terms.

The recurring parameters in this mathematical model are:

- $\alpha$ : Linewidth Enhancement Factor, equal to 3 in our case;

- $\tau_{IN}$ : RSOA cavity roundtrip time;
- $N_S$ : stationary solution for carrier density;
- $g_N$ : modal gain coefficient, equivalent to  $38\text{cm}^{-1}$ ;
- $r_R(\omega_S)$ : total reflection coefficient, considering both RSOA and Silicon Photonic section evaluated at the frequency of the chosen stationary solution;
- $t_{SSC}$ : spot size converter transmission coefficient;
- $T_{c,out}$ : power output coupler coefficient equal to 0.73;
- $\tau_{IN,SiN}$ : time delay related to the path of the light in the straight waveguide of the  $Si_3N_4$  section;
- $\gamma_{c1,2}$ : this is the rate at which the electric field is coupled from the bus waveguide into the ring;
- $\gamma_{t1,t2}$ : this is, instead, the rate at which the electric field is lost, going from the ring to the bus waveguide;
- $L$ : is the RSOA length,  $0.1\text{cm}$ ;
- $\eta_i$ : internal quantum efficiency, corresponding to 0.76;
- $\sigma$ : it is a coefficient that accounts for the electric field average along propagation through the RSOA.

In this configuration, the rates that accounts for the electric field coupling and loss from/to rings, are defined as:

$$\gamma_{c1,2} = \frac{v_{g1,2} k_{RR} (1 - \eta)}{2\pi R_{1,2} t_{RR} A_{loss1,2}^{1/4}} \quad (3.6)$$

Where  $\eta$  is a coefficient that quantifies the Power Coupling losses,  $A_{loss1,2}$  identifies the ring losses, and  $R$  represent the ring radius.

In order to perform dynamic simulations of the device under test, the set of equations given by (3.1, 3.3-3.5) is implemented in Matlab, in a slight different form:

$$E(t) = \frac{e^{j(\omega_s - \omega_0)\tau_{IN}} \exp(f(\omega_s, N_s))}{r_R(\omega_s)} A^-(t - \tau_{IN}) + F(t) \quad (3.7)$$

$$\frac{dA_{c1}(t)}{dt} = \gamma_{c1} t_{SSC}^2 (1 - T_{c,out}) E(t - \tau_{IN, SiN}) e^{(-j\Delta\phi)} - \gamma_{t1} A_{c1}(t) \quad (3.8)$$

$$\frac{dA_{c2}(t)}{dt} = \gamma_{c2} A_{c1}(t) - \gamma_{t2} A_{c2}(t) \quad (3.9)$$

$$\frac{dN(t)}{dt} = \frac{\eta_i I}{qV} - \frac{N(t)}{\tau_N} - v_g g_N \ln\left(\frac{N(t)}{N_0}\right) \sigma \frac{|E(t)|^2}{V} \quad (3.10)$$

Where:

$$A^-(\omega - \omega_0) = r_R E(\omega - \omega_0) \quad (3.11)$$

$$f(\omega_s, N_s) = \frac{1}{\tau_{IN}} \int_{t-\tau_{IN}}^t L \left(1 + j\alpha \frac{\omega_s}{\omega_0}\right) g_N \ln\left(\frac{N(\bar{t})}{N_s}\right) d\bar{t} \quad (3.12)$$

The different parametrization of this model for its implementation affects also the coefficient  $\gamma_c$ , in fact:

$$\gamma_{c1,2} = \frac{\sqrt{k_1 k_2} A_{loss1,2}^{1/4} v_{g1,2}}{A_{loss1,2}^{1/2} \sqrt{1 - k_1} \sqrt{1 - k_2} 2\pi R_{1,2}} \quad (3.13)$$

### 3.3 Dynamical Simulations

The dynamic simulations have been carried out using the numeric computing environment *Matlab*, considering the previous mentioned parameters conveniently modified, in order to investigate the behaviour of the Laser under exam, for varying values of the Laser's effective reflectivity FWHM, the phase shift, the bias current and the power coupling coefficient of the rings. The purpose of this parameter investigation is to find a suitable region which allows to have good performances in many application fields.

In this section are reported these analyses, explaining how these are implemented and the meaning of the output results.

### 3.3.1 Intensity Modulation response

Despite the laser is usually defined as light source, a possible alternative definition could be also as a sort of active electro-optic converter, in the sense that it shows light amplification of a positive factor, which produces an output optical power when there is a bias current flowing.

The IM response is the most important expression of this phenomenon, representing a figure of merit of how the laser responds in power to a given current intensity modulation.

In this specific scenario, the simulation has been performed with a current step around  $104mA$ .

In Figure(3.2) is depicted the IM response to the aforementioned current step. These curves are obtained adjusting the detuning factor, tuning it to the effective reflectivity peak,  $\Delta\nu$  to be equal to  $-0.33GHz$  for different laser's FWHM. In order to change the value of the FWHM the power coupling coefficient of the rings has been changed accordingly.

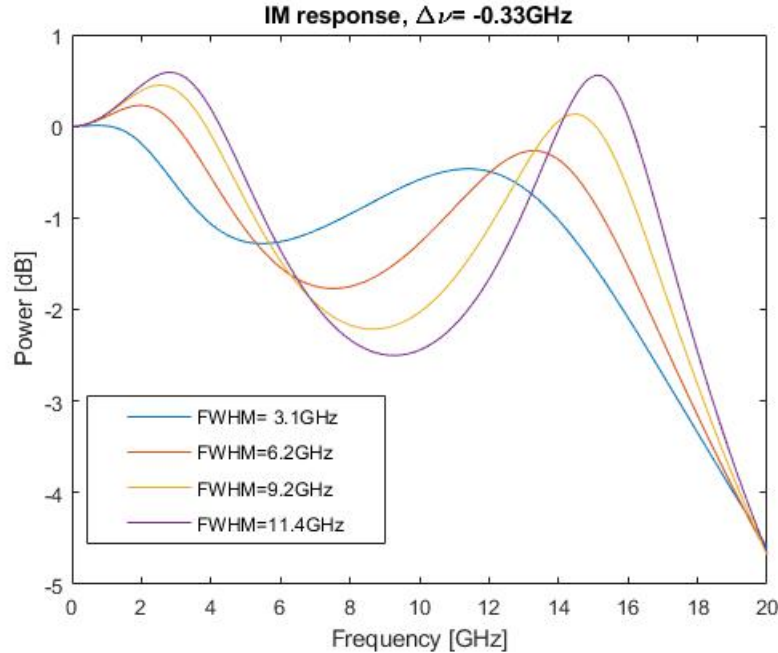


Figure 3.2: IM response for different FWHM.

The numerical relation between the FWHM and the power coupling coefficients

is shown in Table(3.1).

The two peaks of each curve are associated to different phenomena, the first one

Table 3.1: Relation Power coupling coefficient and FWHM

Power Coupling Coefficient ( $k_{RR}$ )	FWHM in GHz
0.051	3.1
0.1	6.2
0.143	9.2
0.173	11.4

is associated to the relaxation oscillation, the second one instead to the Photon-Photon-Resonance, due to the competition of longitudinal modes in the cavity. It is clear that increasing the reflectivity bandwidth the second peak becomes more prominent, due to the increased mode competition. Indeed, when the reflectivity increase, the other longitudinal modes of the cavity are less suppressed. Figure(3.3)

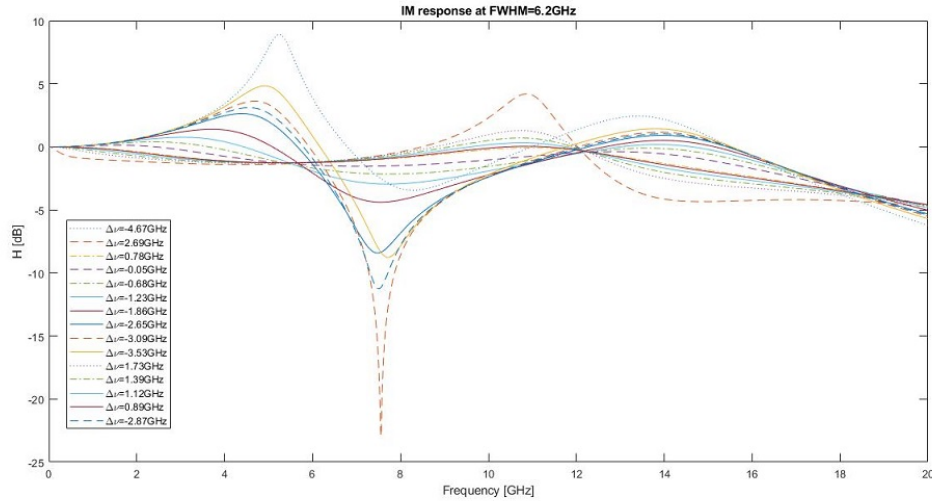


Figure 3.3: IM response at FWHM=6.2GHz for different values of  $\Delta\nu$

shows the IM response of the laser with the FWHM of 6.2GHz, for varying the phase coefficient from 0 to  $2\pi$ , which produces a non-linear variation in the detuning factor. In particular, for certain values of  $\Delta\phi$ ,  $\Delta\nu$  becomes positive, the further this value

is from zero, more the two peaks become accentuated. It is clear that for negative values of detuning factor, the closer this value is to zero, the flatter the response will be. In particular, the flattest IM response associated to FWHM=6.2GHz is obtained with a value of the detuning factor  $\Delta\nu = -0.68GHz$ . Here following are

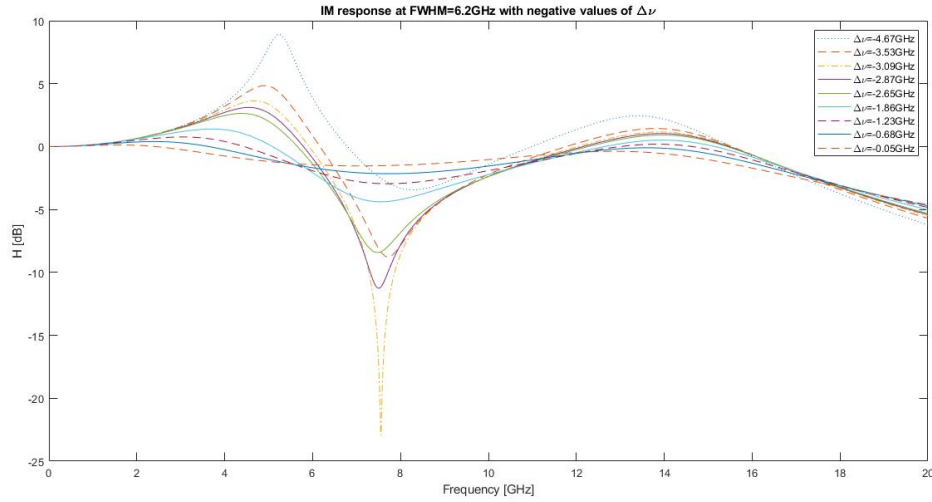


Figure 3.4: IM response at FWHM=6.2GHz for negative values of  $\Delta\nu$

reported also the two plots considering respectively only negative (Fig.3.4) , and positive (Fig.3.5) values of the detuning factor.

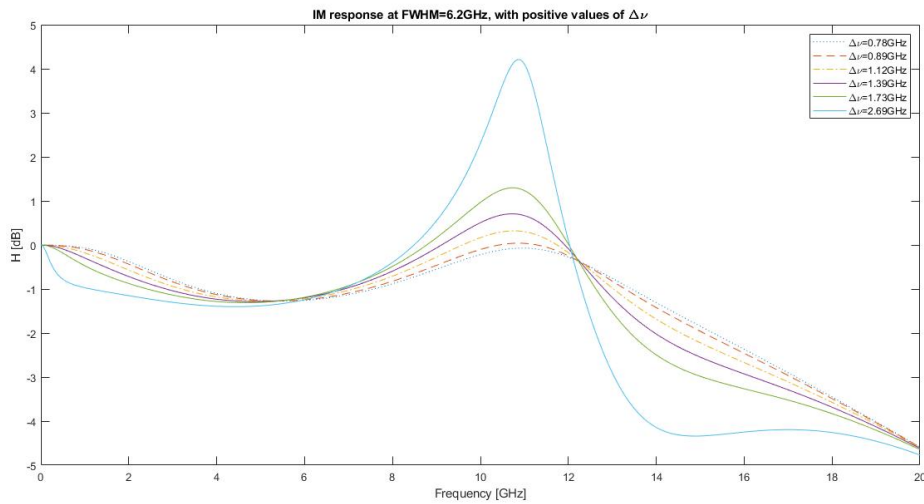


Figure 3.5: IM response at FWHM=6.2GHz for positive values of  $\Delta\nu$

Reducing the power coupling coefficient of the rings down to 0.018, the FWHM is reduced to 1 GHz. In Figure(3.6) is shown the IM response of the hybrid laser for this specific case.

It can be noticed that in this case the peak relative to the Photon Photon Resonance is reduced to a minimum, due to the very narrow reflective region, leading to the laser to have an almost single-mode stability, still having mode competition but extremely reduced.

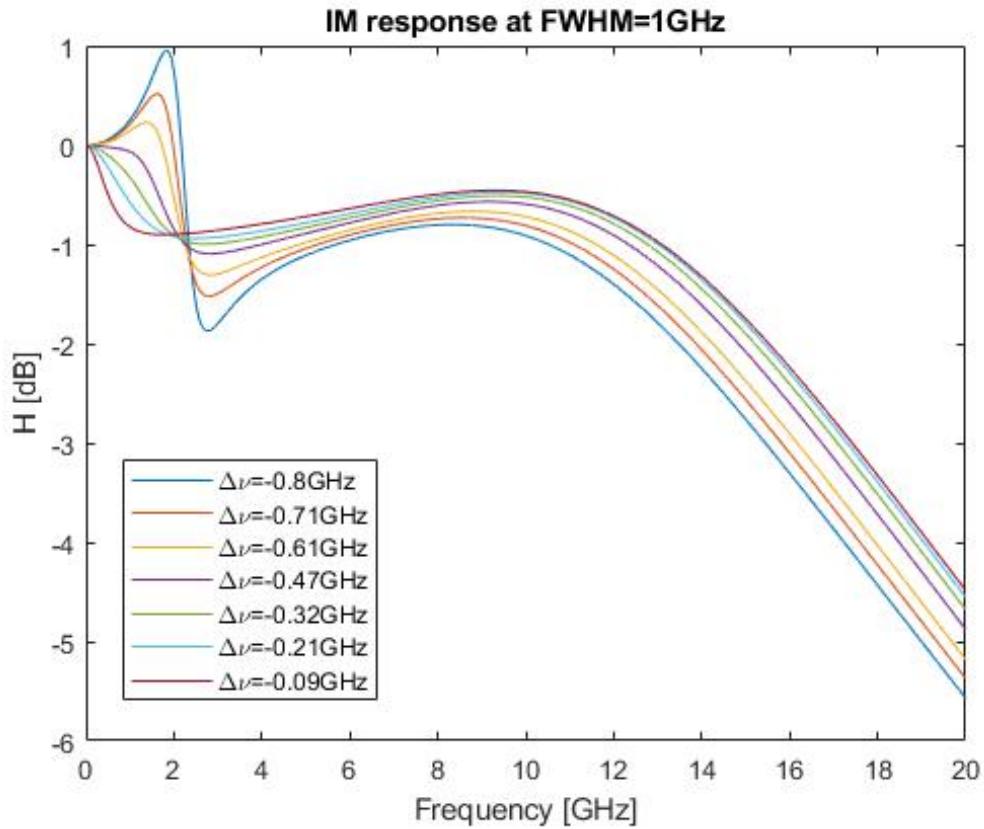


Figure 3.6: IM response at FWHM=1GHz for different values of  $\Delta\nu$ .

On the contrary, increasing the value of  $k_{RR}$  as reported in Table(3.1), or even more with  $k_{RR} = 0.28$  in order to have  $FWHM = 20.3GHz$  the IM response changes deeply.

Indeed, in Figure(3.7) and Figure(3.8), where are reported the IM response for lasers with FWHM=9GHz and FWHM=11GHz respectively, the second peak starts

to become relevant, since there is enough space to allow mode competition in the cavity. This is accentuated even more in Figure(3.9), in which the second peak is the predominant.

In Figure(3.8) and Figure(3.9), there is a thicker line, this represents the most flat IM response, associated respectively to detuning factors:  $\Delta\nu = -0.06$  and  $\Delta\nu = -0.08$ .

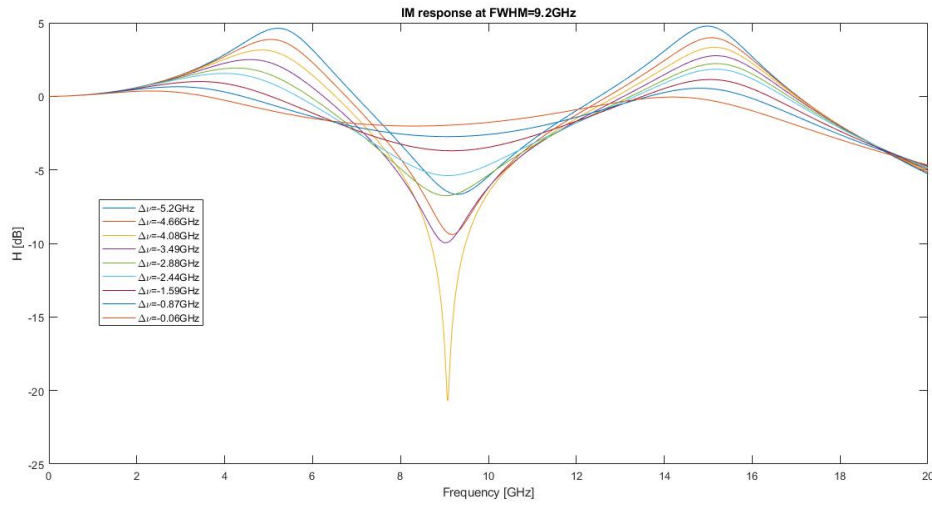


Figure 3.7: IM response at FWHM=9GHz for different values of  $\Delta\nu$ .

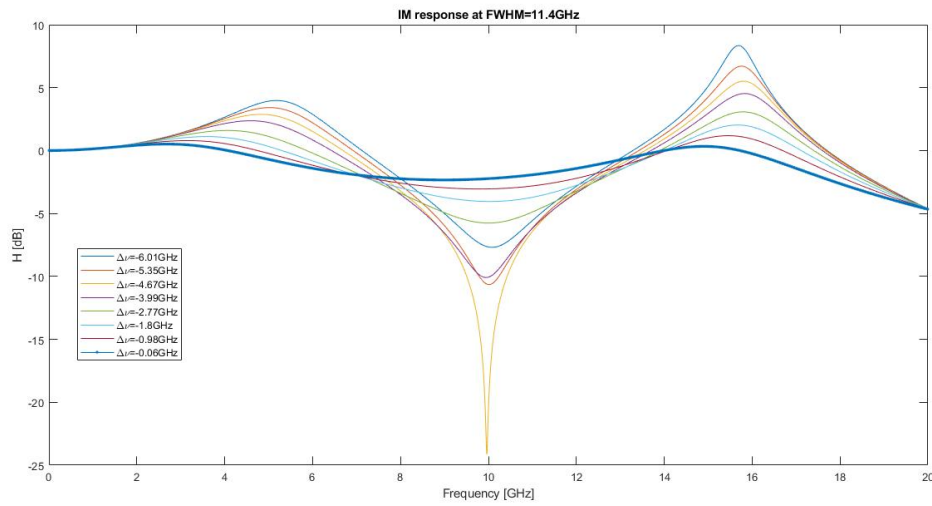


Figure 3.8: IM response at FWHM=11GHz for different values of  $\Delta\nu$ .

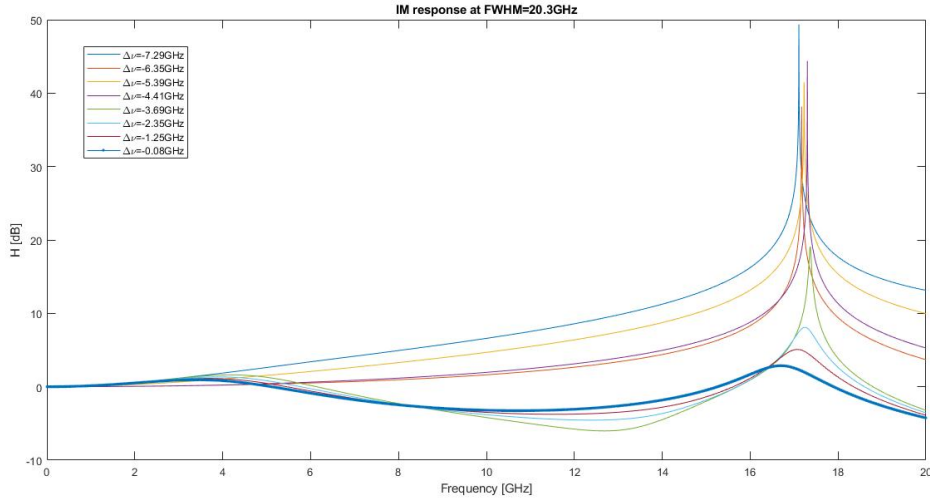


Figure 3.9: IM response at FWHM=20GHz for different values of  $\Delta\nu$ .

### 3.3.2 Relative Intensity Noise (RIN) spectrum

After the IM response, the laser has been simulated to obtain its Relative Intensity Noise spectrum, which is a measure of the noise of the optical intensity, or power, which is then normalized to its average value.

Hereafter are reported only the most relevant plot of the simulations, which shows how by changing the laser parameters it is possible to obtain a behaviour that goes from stability to instability. In particular, these Figures are obtained with three different values of detuning factor, while maintaining the same FWHM=6.2GHz.

Each of these figures is obtained mapping the RIN for 30 values of current  $I_{bias}$  from 30mA to 250mA, considering fixed the detuning factor, plotting the RIN spectrum (colormap) expressed in dBc/Hz as a function of Frequency (x-axis) and current (y-axis).

In Figure(3.10), the detuning factor is  $\Delta\nu = -2.65GHz$  and it is possible to notice that the laser does not show any instability point, for each frequency, since the RIN remains below -160dBc/Hz.

In this Figure it is also possible to distinguish the two peaks associated respectively to the Relaxation Oscillation and to the Photon-Photon-Resonance, identified by the yellow traces.

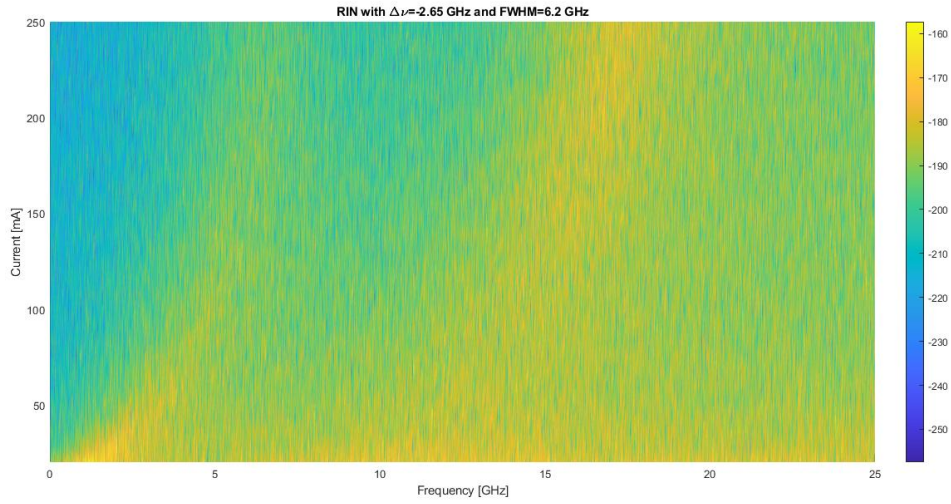
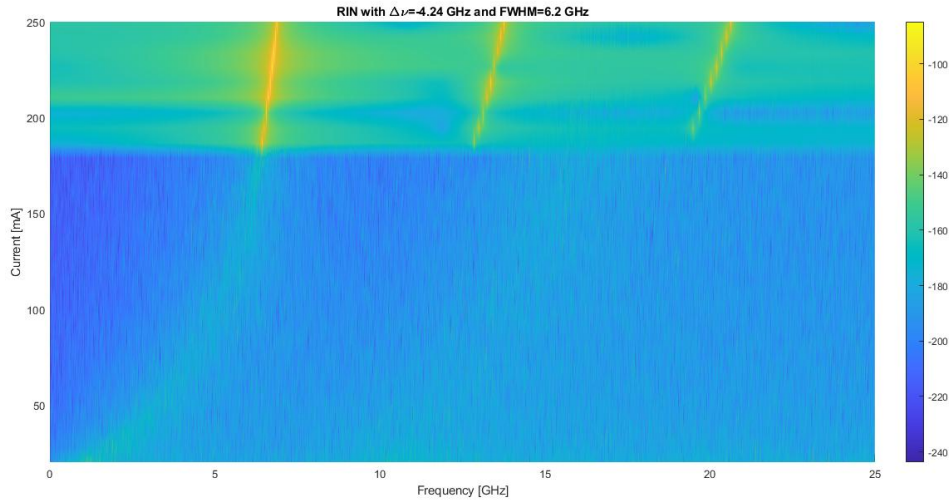


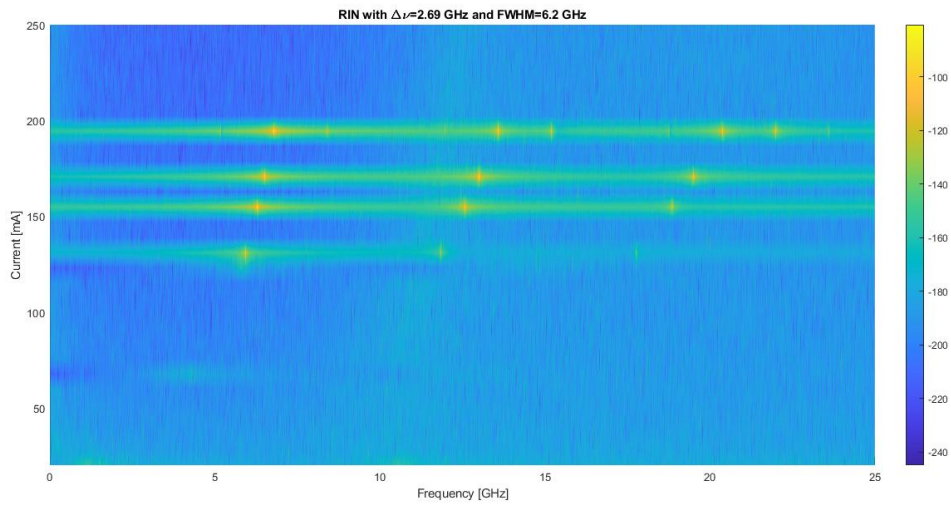
Figure 3.10: RIN spectrum for  $\Delta\nu = -2.65GHz$

In Figure(3.11) the simulation shows a different result with respect to the previous one, in fact, for current above 180 mA, at frequencies above 5GHz there are three peaks, that identify the beating of the lasing mode with other longitudinal modes of the cavity. The first yellow peak of the RIN is linked to the relaxation oscillations, that after a certain value become undamped, the others are related to the harmonics. This happens because the frequency of relaxation oscillation is resonant with the beating of two longitudinal modes of the cavity. [20]

The most important difference between Figure(3.11) and Figure(3.10) is that in this case there is a higher value of detuning factor, entering in an un-stable regime.

Figure 3.11: RIN spectrum for  $\Delta\nu = -4.24GHz$ 

In Figure(3.12) it is visible the behaviour of the laser with detuning factor of  $2.69GHz$ , where is present the mode-hopping phenomenon, which under certain conditions lets the laser discontinuously switch the wavelength back and forth in frequency thus showing a non-uniform RIN map.

Figure 3.12: RIN spectrum for  $\Delta\nu = 2.69GHz$

### 3.3.3 Integrated RIN

Finally we show the behaviour of the integrated RIN over a bandwidth of 25 GHz by sweeping 30 values of bias current  $I_{bias}$  from  $30mA$  to  $250mA$ , and 30 values of detuning factor, obtained through 30 values of  $\Delta\phi$ .

In each of the plot reported is clearly visible a blue area and a yellow one. The blue region identifies a stable single-mode regime, while the yellow region shows the multimode regime.

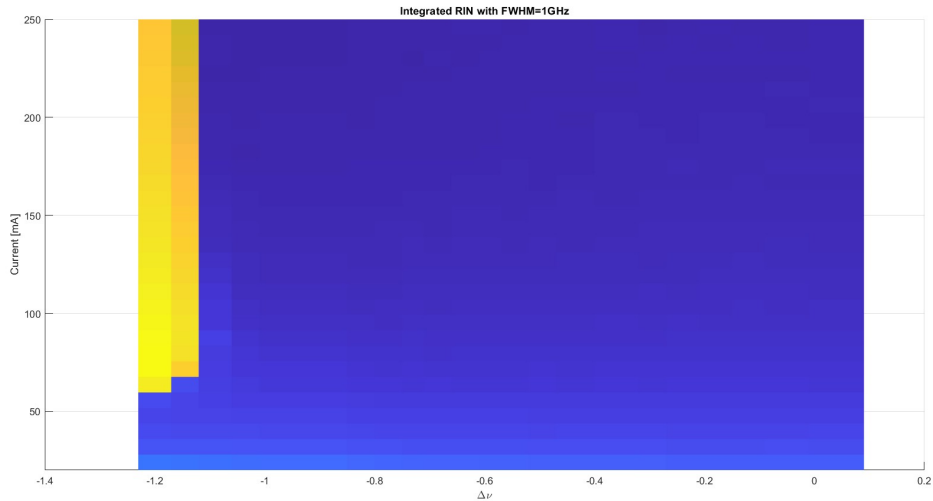


Figure 3.13: Integrated RIN for FWHM=1GHz

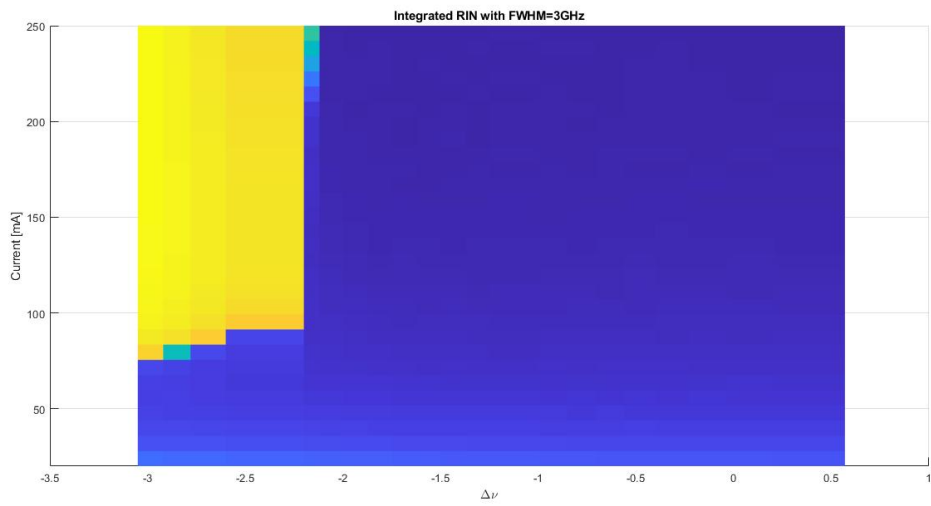


Figure 3.14: Integrated RIN for FWHM=3GHz

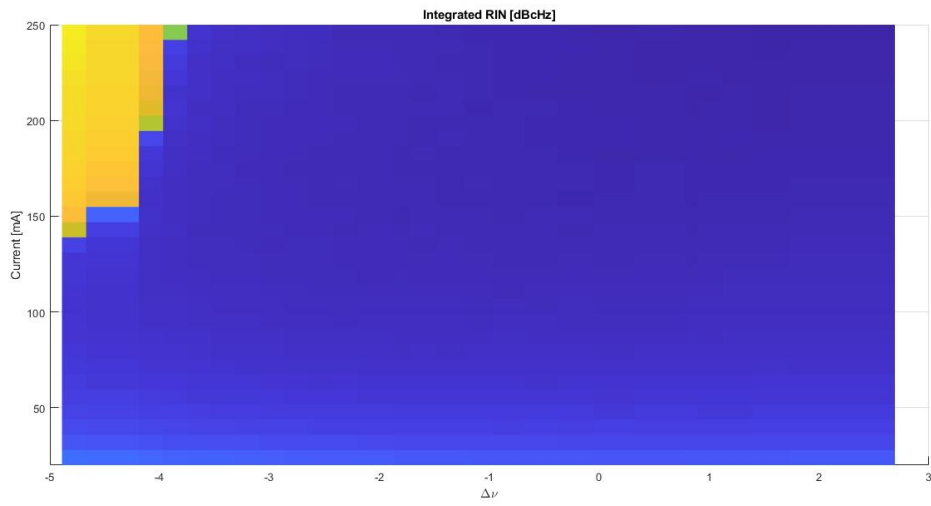


Figure 3.15: Integrated RIN for FWHM=6.2GHz

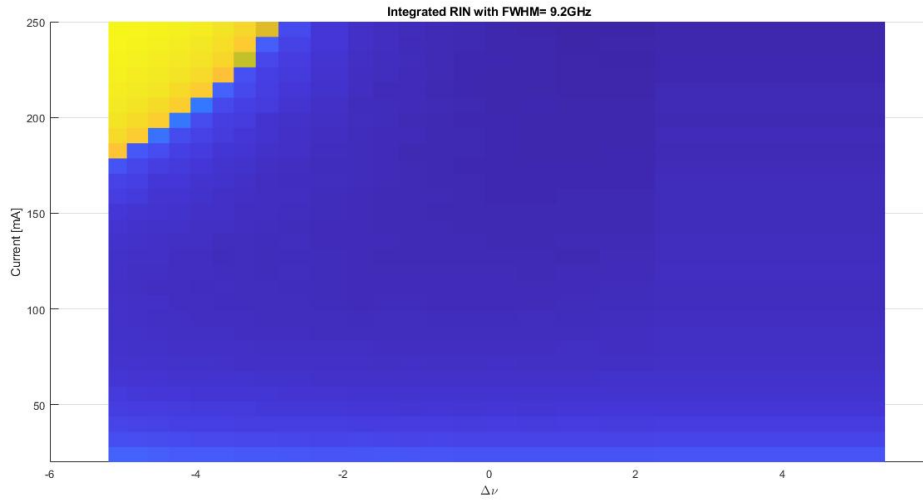


Figure 3.16: Integrated RIN for FWHM=9GHz

From these figures it can be noticed that the larger is the FWHM, the larger in frequency will be the unstable yellow region, due to the fact that there is more reflective region in which there could be competition between lasing mode and other longitudinal modes of the cavity. In fact, as mentioned before, the cause of instability is to ascribe to the relaxation oscillations that become undamped leading to resonance.

### 3.3.4 Eye Diagram

In this section are reported the plots of the Eye diagram simulation, that is the representation of the goodness of a signal for communication purposes.

In this specific case it has been considered a square wave like bias current, with the minimum and maximum intensity values chosen to guarantee a ratio of power of about  $10dB$ , in particular choosing  $I_{LOW} = 65mA$  and  $I_{HIGH} = 145mA$ . These simulation are carried out considering a FWHM=6.2 GHz and the flattest IM response corresponding to it, properly choosing the value of the detuning factor  $\Delta\nu = -0.68GHz$ .

In Figure(3.17) the eye diagram resulting from a frequency modulation of the current of 10 GHz is depicted, in which the Laser already assumes a correct on-off

behaviour, allowing for the eye to be almost fully open, i.e. resulting in the perfect time to sample the signal.

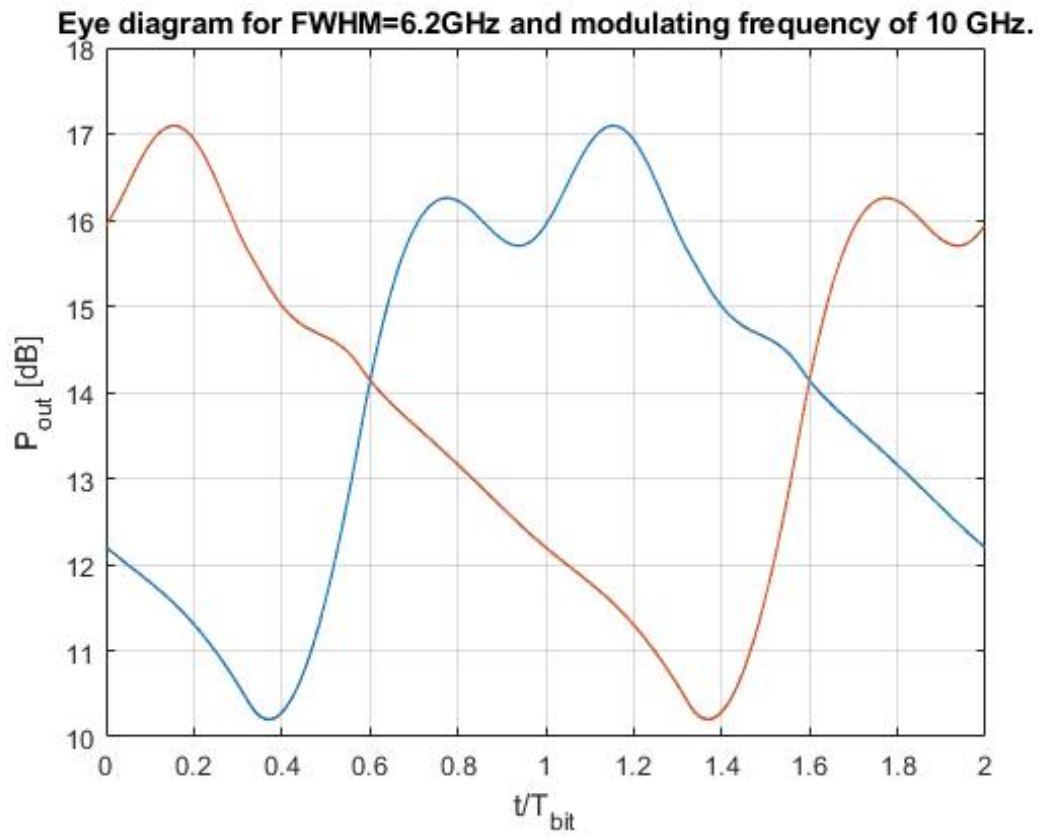


Figure 3.17: Eye Diagram with modulation frequency of 10 GHz.

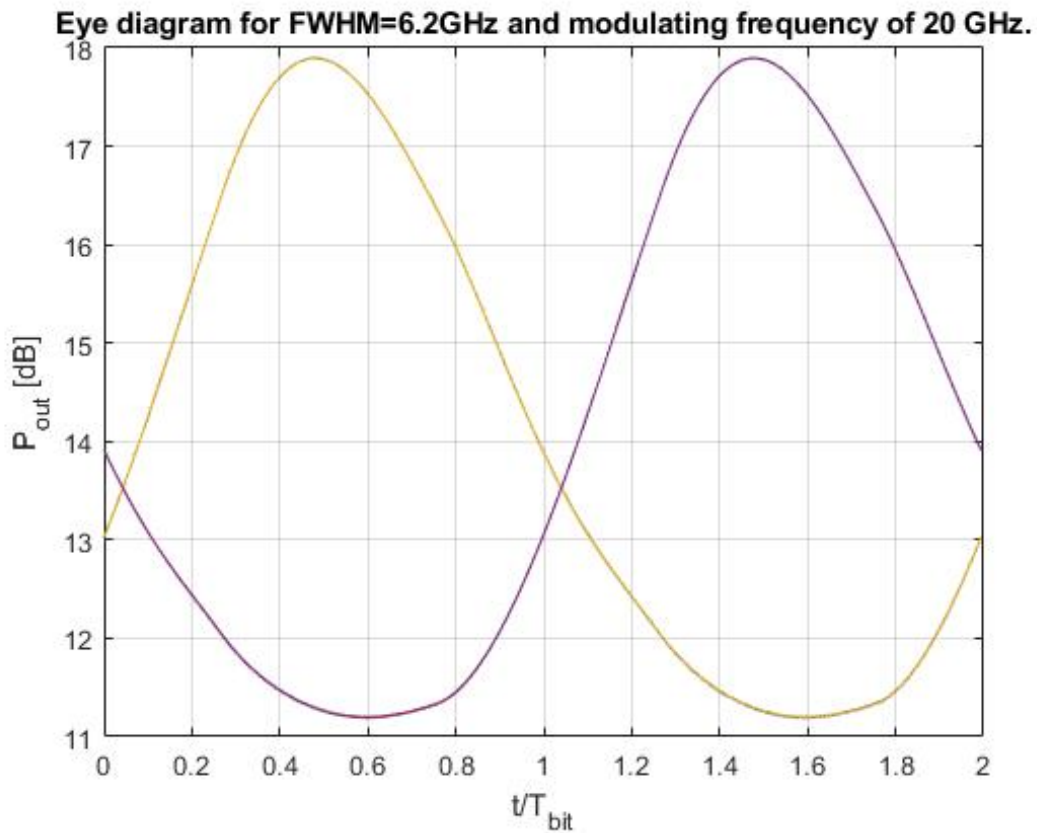


Figure 3.18: Eye Diagram with modulation frequency of 20 GHz.

In Figure(3.18) and Figure(3.19) are reported the plots for the eye diagrams referred to the same square wave modulating current of Figure(3.17), but considering a modulating frequency of 20GHz and 30 GHz respectively. It can be noticed that at the increasing of the frequency, the eye results to be more open, allowing for a better sampling of the optical signal.

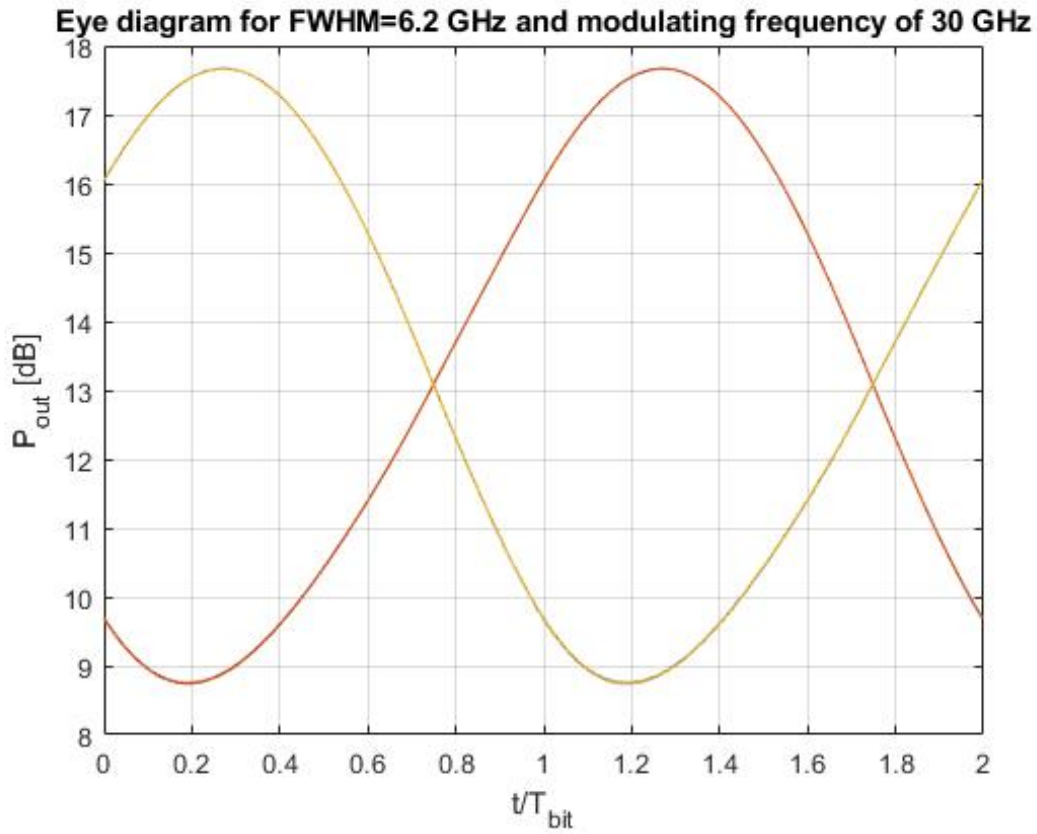


Figure 3.19: Eye Diagram with modulation frequency of 30 GHz.

In this section instead of the square wave modulating current with fixed periods, has been considered a Pseudo Random Bit Stream of current, with a modulating frequency of 10 GHz.

The PRBS has been implemented in *Matlab* through a pre-formed function, which relies on polynomial functions, choosing an 8-degree polynomial, the high value of the current is  $I_{bias,high} = 200mA$ , while the low value of the current is  $I_{bias,low} = 100mA$ . This current is shown in Figure(3.20), with a closeup in Figure(3.21), from which is possible to notice its random shape.

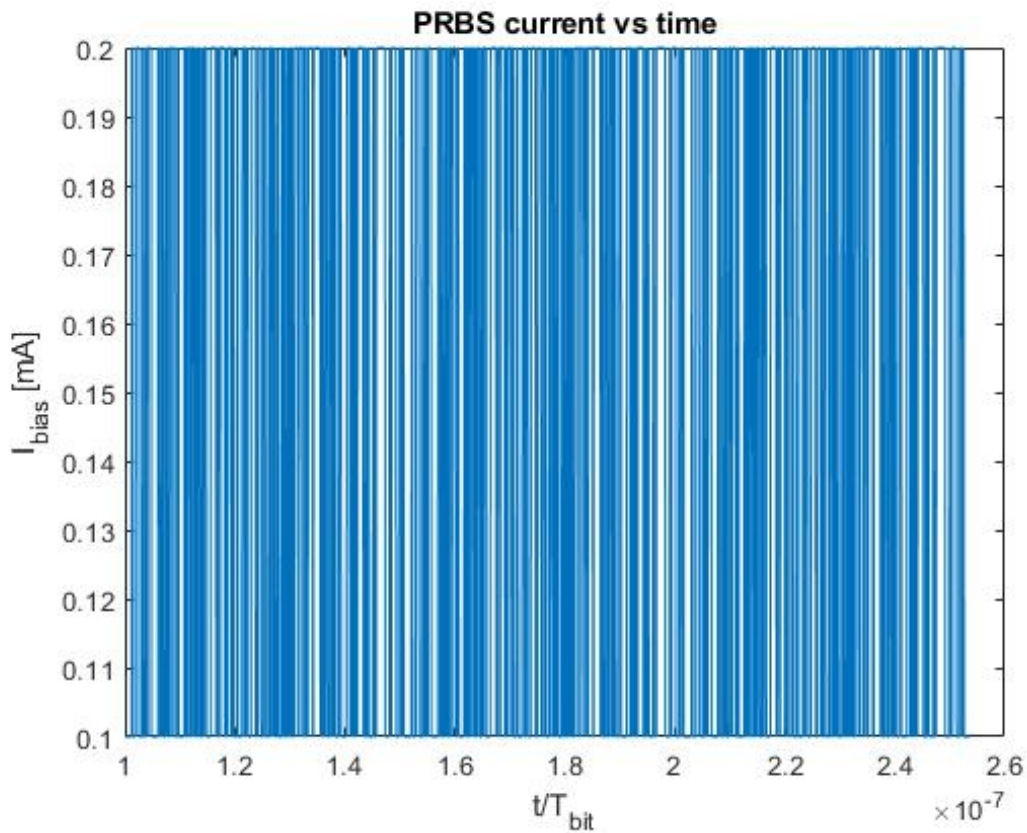


Figure 3.20: Current vs Time.

The resulting eye diagram is depicted in Figure(3.22). It results clear that in this case, with respect to the previous one, the output plot is less clean, this is due to the simulation of a more realistic situation in which the communication signal is not a square wave with fixed path low-high with fixed period, but has a different shape. Every different colour of the curves in Figure(3.22) represents different time slices in which the output power is divided.

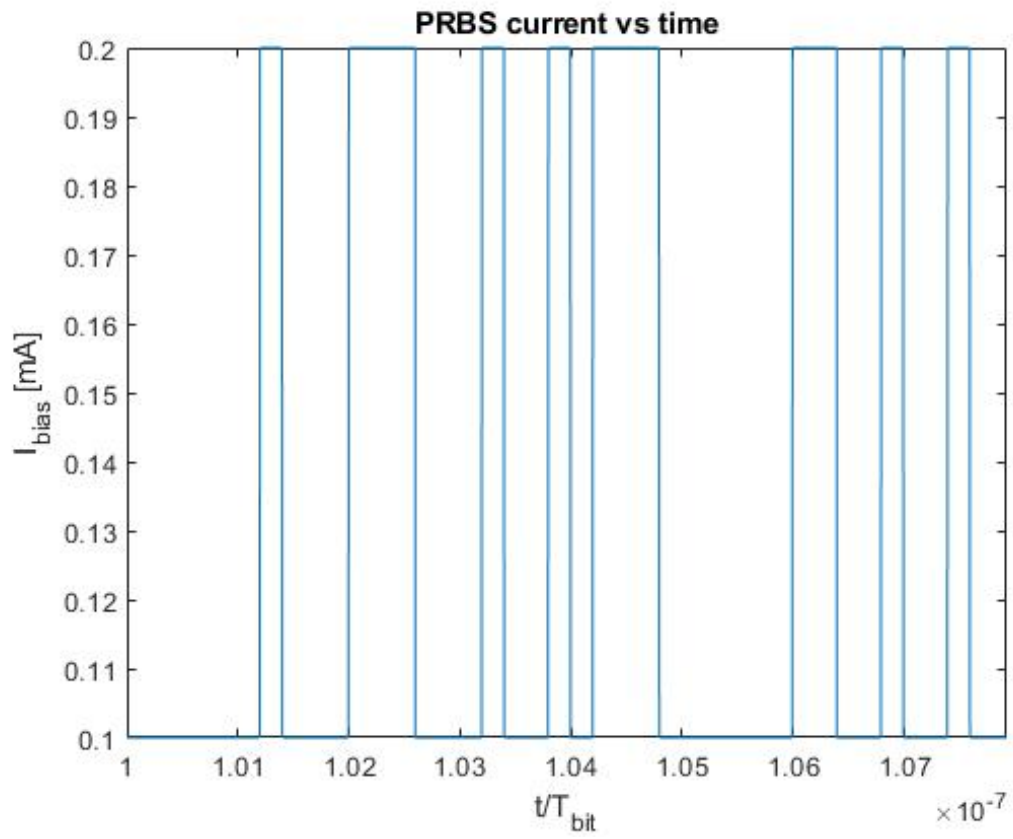


Figure 3.21: Closeup of the previous current vs time plot.

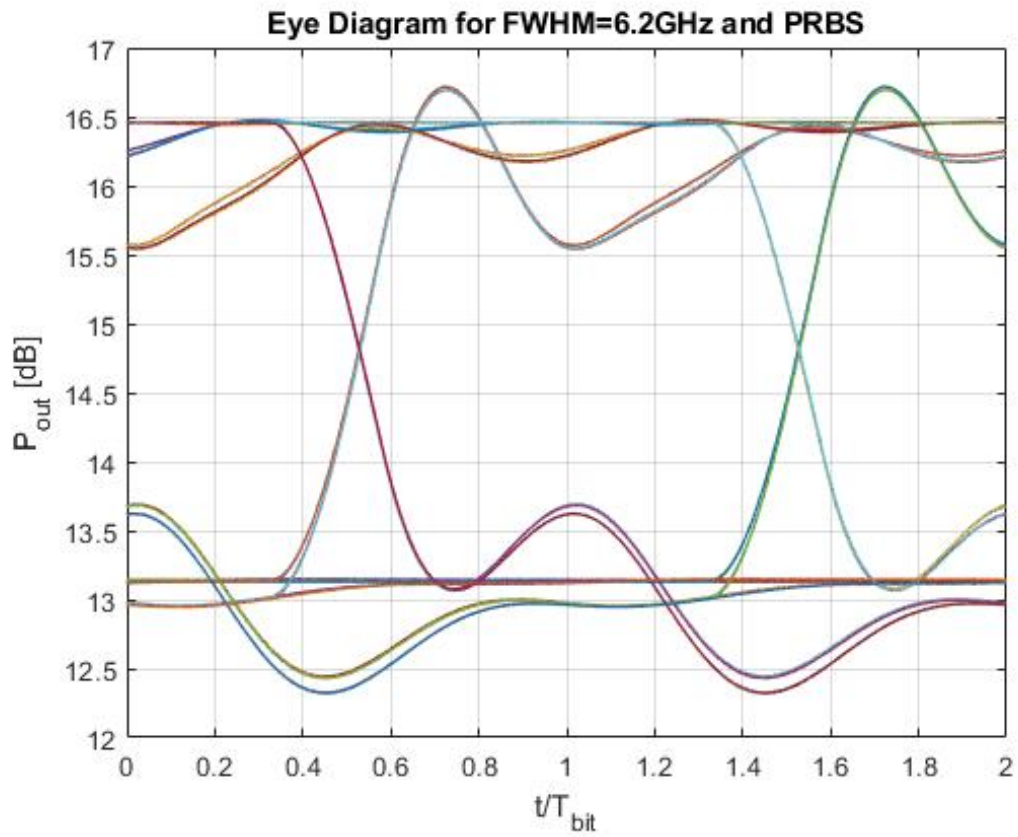


Figure 3.22: Eye Diagram with Pseudo Random Bit Stream of Current and Frequency=10GHz.

# Chapter 4

## Conclusions

The main focus of this thesis is to prove the feasibility and investigate the performances of a Laser using Silicon Photonic technologies. This means that the attention is moved firstly over the actual Silicon Photonics strategies of integration, considering the already proved CMOS technology as example and base of knowledge.

In particular, studying and analysing the actual electronic circuits integration State of the Art, it is possible to choose between the Monolithic Integration, Heterogeneous Integration and Hybrid Integration as three valid alternatives to proceed in the direction of a future for the optical integration itself.

These three alternatives show each benefits and drawbacks, linked to geometry and/or physical limitations. In particular, as expressed in Chapter 1, the most important feature of the Monolithical integration is that the goal is to have both electronic and optical components integrated on the same semiconductor wafer, on the other hand, results to be very challenging to reach this purpose, due to the difficulties of having the integration of light sources, i.e. the need of having a large enough band-gap is the main drawback of this technology.

Concerning the Heterogeneous integration, which consists in the bonding of an already proved III-V die on which lie the optical components, over a Silicon platform, it results in high performances devices benefiting of the best possible implementation of optical components and at the same time granting the best solution of integrability for the electronic parts. Unfortunately, this technology requires a big amount of area of the original Silicon wafer, increasing costs and also leading to poor thermal performances, due to the increase of the thermal resistance, which is the result of having the superposition of the III-V die over the wafer.

The last and, up to now, best solution is the Hybrid integration, which relies on the coupling of optical components with the Silicon Photonic platform. The difficulties are introduced by the necessity of a perfect alignment of these two sections, but the

benefits help to make up for this drawback. Indeed, this strategy benefits from the characteristics and full performances of the optical components, that are already implemented without the necessity of the integration over the Photonic layer, with all the related problems.

For this reason this is the choice of most implementations of Laser in Silicon Photonics. In fact, in Chapter 2 are taken as example two important research groups, which exploits the heterogeneous and hybrid integration to fabricate Lasers with high performances in terms of narrow linewidth and optical power output. The choice of analysing the work of these groups lies on the fact that the structures used to reach the goal are very similar to the structure proposed in Chapter 3. It can be noticed, in fact, that in each of the work reported the resonant cavity contains ring resonators, which results to be suitable and effective for the generation of frequency comb, narrowing of the linewidth and large range of tunability.

The structure proposed in Chapter 3 is an hybrid integrated laser, which has been simulated in Matlab and results has been commented. The outcome of this analysis is that the proposed structure is satisfactory in terms of performances, and due to its proved integrability, it can be taken into account as a valid solution for Silicon Photonics. Indeed, from the dynamic point of view, the device shows good performances in terms of IM response and possibly for communication purposes.

This thesis work could be extended in future in order to provide proofs of its integrability in a pure Silicon layer, in order to benefit from the low-cost fabrication of Silicon chip platforms, allowing for a perfect CMOS-process compatibility and also for the suitability of Silicon in optical communications, since it shows the transparency at wavelengths higher than  $1.1\mu m$ .

Indeed, it will be a point of interest to consider non-linear effects arising from this choice of material, as the already mentioned Two Photon Absorption and Kerr effect, which here are not taken into account.

# Bibliography

- [1] Jia-ming Liu. *Photonic Devices*. Cambridge University Press, Apr. 2005. DOI: [10.1017/cbo9780511614255](https://doi.org/10.1017/cbo9780511614255). URL: <https://doi.org/10.1017/cbo9780511614255>.
- [2] Minhaz Abedin. “A Self-Adjusting Lin-Log active pixel for wide dynamic range CMOS image sensor”. PhD thesis. Oct. 2015. DOI: [10.13140/RG.2.1.3871.8965](https://doi.org/10.13140/RG.2.1.3871.8965).
- [3] Giovanni Ghione. *Semiconductor Devices for High-Speed Optoelectronics*. Cambridge University Press, Oct. 2009. DOI: [10.1017/cbo9780511635595](https://doi.org/10.1017/cbo9780511635595). URL: <https://doi.org/10.1017/cbo9780511635595>.
- [4] J.J.G.M. van der Tol et al. “InP-based photonic circuits: Comparison of monolithic integration techniques”. In: *Progress in Quantum Electronics* 34.4 (July 2010), pp. 135–172. DOI: [10.1016/j.pquantelec.2010.02.001](https://doi.org/10.1016/j.pquantelec.2010.02.001). URL: <https://doi.org/10.1016/j.pquantelec.2010.02.001>.
- [5] Meint K. Smit. “Past and future of InP-based Photonic Integration”. In: *LEOS 2008 - 21st Annual Meeting of the IEEE Lasers and Electro-Optics Society*. IEEE, Nov. 2008. DOI: [10.1109/leos.2008.4688483](https://doi.org/10.1109/leos.2008.4688483). URL: <https://doi.org/10.1109/leos.2008.4688483>.
- [6] Vladimir Stojanović et al. “Monolithic silicon-photonic platforms in state-of-the-art CMOS SOI processes [Invited]”. In: *Optics Express* 26.10 (May 2018), p. 13106. DOI: [10.1364/oe.26.013106](https://doi.org/10.1364/oe.26.013106). URL: <https://doi.org/10.1364/oe.26.013106>.
- [7] Tin Komljenovic et al. “Heterogeneous Silicon Photonic Integrated Circuits”. In: *Journal of Lightwave Technology* 34.1 (Jan. 2016), pp. 20–35. DOI: [10.1109/jlt.2015.2465382](https://doi.org/10.1109/jlt.2015.2465382). URL: <https://doi.org/10.1109/jlt.2015.2465382>.
- [8] Aleksandr Biberman et al. “Ultralow-loss silicon ring resonators”. In: *Optics Letters* 37.20 (Oct. 2012), p. 4236. DOI: [10.1364/ol.37.004236](https://doi.org/10.1364/ol.37.004236). URL: <https://doi.org/10.1364/ol.37.004236>.

- [9] Muhammad Rodlin Billah et al. “Hybrid integration of silicon photonics circuits and InP lasers by photonic wire bonding”. In: *Optica* 5.7 (July 2018), p. 876. DOI: [10.1364/optica.5.000876](https://doi.org/10.1364/optica.5.000876). URL: <https://doi.org/10.1364/optica.5.000876>.
- [10] *SOITEC SOI wafer Smart Cut*. URL: <https://www.soitec.com/en/products/smart-cut>.
- [11] Kerstin Wörhoff et al. “TriPleX: a versatile dielectric photonic platform”. In: *Advanced Optical Technologies* 4.2 (Jan. 2015). DOI: [10.1515/aot-2015-0016](https://doi.org/10.1515/aot-2015-0016). URL: <https://doi.org/10.1515/aot-2015-0016>.
- [12] Duanni Huang et al. “High-power sub-kHz linewidth lasers fully integrated on silicon”. In: *Optica* 6.6 (May 2019), p. 745. DOI: [10.1364/optica.6.000745](https://doi.org/10.1364/optica.6.000745). URL: <https://doi.org/10.1364/optica.6.000745>.
- [13] Minh A. Tran et al. “Ring-Resonator Based Widely-Tunable Narrow-Linewidth Si/InP Integrated Lasers”. In: *IEEE Journal of Selected Topics in Quantum Electronics* 26.2 (Mar. 2020), pp. 1–14. DOI: [10.1109/jstqe.2019.2935274](https://doi.org/10.1109/jstqe.2019.2935274). URL: <https://doi.org/10.1109/jstqe.2019.2935274>.
- [14] E. Patzak et al. “Semiconductor laser linewidth in optical feedback configurations”. In: *Electronics Letters* 19.24 (1983), p. 1026. DOI: [10.1049/el:19830695](https://doi.org/10.1049/el:19830695). URL: <https://doi.org/10.1049/el:19830695>.
- [15] R F Kazarinov and C H Henry. “The relation of line narrowing and chirp reduction resulting from the coupling of a semiconductor laser to a passive resonator”. In: *IEEE J. Quant. Electron.; (United States)* (Sept. 1987). DOI: [10.1109/JQE.1987.1073531](https://doi.org/10.1109/JQE.1987.1073531). URL: <https://www.osti.gov/biblio/6131437>.
- [16] Minh A. Tran, Duanni Huang, and John E. Bowers. “Tutorial on narrow linewidth tunable semiconductor lasers using Si/III-V heterogeneous integration”. In: *APL Photonics* 4.11 (Nov. 2019), p. 111101. DOI: [10.1063/1.5124254](https://doi.org/10.1063/1.5124254). URL: <https://doi.org/10.1063/1.5124254>.

- [17] Jesse Mak et al. “Linewidth narrowing via low-loss dielectric waveguide feedback circuits in hybrid integrated frequency comb lasers”. In: *Optics Express* 27.9 (Apr. 2019), p. 13307. DOI: [10.1364/oe.27.013307](https://doi.org/10.1364/oe.27.013307). URL: <https://doi.org/10.1364/oe.27.013307>.
- [18] Youwen Fan et al. “Hybrid integrated InP-Si<sub>3</sub>N<sub>4</sub> diode laser with a 40-Hz intrinsic linewidth”. In: *Opt. Express* 28.15 (July 2020), pp. 21713–21728. DOI: [10.1364/OE.398906](https://doi.org/10.1364/OE.398906). URL: <https://opg.optica.org/oe/abstract.cfm?URI=oe-28-15-21713>.
- [19] Cristina Rimoldi et al. “Damping of relaxation oscillations, photon-photon resonance, and tolerance to external optical feedback of III-V/SiN hybrid lasers with a dispersive narrow band mirror”. In: *Optics Express* 30.7 (Mar. 2022), p. 11090. DOI: [10.1364/oe.452155](https://doi.org/10.1364/oe.452155). URL: <https://doi.org/10.1364/oe.452155>.
- [20] Cristina Rimoldi et al. “CW Emission and Self-Pulsing in a III-V/SiN Hybrid Laser With Narrow Band Mirror”. In: *IEEE Photonics Journal* 14.4 (Aug. 2022), pp. 1–7. DOI: [10.1109/jphot.2022.3188202](https://doi.org/10.1109/jphot.2022.3188202). URL: <https://doi.org/10.1109/jphot.2022.3188202>.